INNATE LYMPHOID CELLS

Pulmonary environmental cues drive group 2 innate lymphoid cell dynamics in mice and humans

Franz Puttur[1]*, Laura Denney[1]*, Lisa G. Gregory[1], Juho Vuononvirta[1], Robert Oliver[1], Lewis J. Entwistle[1], Simone A. Walker[1], Mark B. Headley[2], Ewan J. McGhee[3], James E. Pease[1], Matthew F. Krummel[4], Leo M. Carlin[1,3,5†], Clare M. Lloyd[1†]

Group 2 innate lymphoid cells (ILC2s) are enriched in mucosal tissues (e.g., lung) and respond to epithelial cell–derived cytokines initiating type 2 inflammation. During inflammation, ILC2 numbers are increased in the lung. However, the mechanisms controlling ILC2 trafficking and motility within inflamed lungs remain unclear and are crucial for understanding ILC2 function in pulmonary immunity. Using several approaches, including lung intravital microscopy, we demonstrate that pulmonary ILC2s are highly dynamic, exhibit amoeboid-like movement, and aggregate in the lung peribronchial and perivascular spaces. They express distinct chemokine receptors, including CCR8, and actively home to CCL8 deposits located around the airway epithelium. Within lung tissue, ILC2s were particularly motile in extracellular matrix–enriched regions. We show that collagen-I drives ILC2 to markedly change their morphology by remodeling their actin cytoskeleton to promote environmental exploration critical for regulating eosinophilic inflammation. Our study provides previously unappreciated insights into ILC2 migratory patterns during inflammation and highlights the importance of environmental guidance cues in the lung in controlling ILC2 dynamics.

INTRODUCTION

Innate lymphoid cells (ILCs) are an emerging family of immune cells that originate from fetal liver and adult bone marrow (BM) progenitors (*1*, *2*). Prenatally, ILC progenitors occupy peripheral sites from mid to late stages of fetal development (*3*) and are detectable in peripheral tissues by embryonic day 15.5 in the mouse (*4*). Although ILCs derive from common lymphoid progenitors, they lack specific antigen receptors and lymphoid cell lineage markers but display diverse effector functions, analogous to T cells (*5*, *6*). On the basis of distinct lineage-determining transcription factors, ILCs segregate into three different subsets—ILC1, ILC2, and ILC3 (*7*–*9*). Each ILC subset mirrors a T helper (T_H) cell subset via the production of T_H cell signature cytokines—interferon-γ (T_H1/ILC1), interleukin-13 (IL-13) (T_H2/ILC2), and IL-17 (T_H17/ILC3)—which act to combat infection by intracellular pathogens, helminths, and extracellular pathogens, respectively (*3*). Anatomically, different ILC subsets are resident in particular barrier and nonbarrier sites (*3*), including the BM, skin, secondary lymphoid organs, peripheral blood, and nonlymphoid tissues. ILC3s are vital for the development of adaptive immune organs in utero; however, after birth, thymic ILC3s are replaced by ILC2s, suggesting that these cells play an important role in the thymic microenivronment (*10*). Among nonlymphoid tissues, ILC2s are enriched in mucosal sites including the lung and small intestine, where they contribute to local tissue immunoregulation, repair, and homeostasis (*11*, *12*). In the mouse lung, ILC2s predominate (*13*) and rapidly expand during the first week of life (*14*, *15*), populating collagen-rich structures associated with medium-sized blood vessels and airways (*14*). In a steady-state, long-term maintenance of ILC2s in peripheral tissues, including the lung, is mainly supported by self-renewal of proliferative local tissue-resident progenitor populations (*4*, *15*–*18*). Recent evidence suggests that intercellular adhesion molecule–1 supports ILC2 development and function during lung inflammation (*19*). However, in T_H2 cell–induced lung inflammation, ILC2s exit the BM (*19*, *20*), and concurrently, numbers are increased in the blood and lung (*21*–*24*). Human and mouse ILC2s express β_2 integrins, and these have been proposed to be involved in cell trafficking because blocking β_2 integrins results in reduced ILC2 numbers in the lung after allergen challenge (*22*). In addition, recent studies have identified a distinct pre-ILC2 population originating in the gut that migrates to the lung and other distal sites giving rise to inflammatory ILC2s (iILC2s) that provide protection during worm infection (*15*). Within the lung, interaction of ILC2s with other immune cell populations is a critical factor for shaping type 2 inflammation (*25*).

Several factors, including the epithelial cell–derived cytokines IL-33, IL-25, and thymic stromal lymphopoietin, contribute to ILC2 activation and function (*26*). Upon activation, ILC2s produce cytokines, including IL-4, IL-5, IL-13, colony-stimulating factor 2 (granulocyte-macrophage colony-stimulating factor), and the epidermal growth factor family member amphiregulin (*13*, *27*–*29*). Lipid mediators, including the arachidonic acid metabolites leukotriene D4, prostaglandin D2 (PGD_2) (*30*, *31*), and sphingosine 1-phosphate (S1P) (*15*), serve as potent regulators of ILC2 activation, accumulation, and function. In contrast, prostaglandin E2 and prostacyclin suppress ILC2 function, inhibiting GATA binding protein 3 (GATA-3), IL-5, and IL-13 expression and decreasing proliferation (*32*, *33*). We have previously demonstrated that epithelial cell–derived transforming growth factor–β1 (TGF-β1) is critical for ILC2 activation and significantly enhances airway ILC2 chemoactivity and movement in vitro (*34*). Thus, ILC2 activation, behavior, and function are regulated by a wide variety of factors.

[1]Inflammation, Repair and Development, National Heart and Lung Institute, Imperial College London, London, UK. [2]Clinical Research Division, Fred Hutchinson Cancer Research Center, Seattle, WA 98109, USA. [3]Cancer Research UK Beatson Institute, Garscube Estate, Bearsden, Glasgow, UK. [4]Department of Pathology, University of California, San Francisco, 513 Parnassus Ave., San Francisco, CA, USA. [5]Institute of Cancer Sciences, University of Glasgow, Glasgow, UK.
*These authors contributed equally to this work.
†Corresponding author. Email: c.lloyd@imperial.ac.uk (C.M.L.); l.carlin@beatson.gla.ac.uk (L.M.C.)

Tissue environments critically control optimal immune responses, coordinating timely and proportionate recruitment, motility, migration, chemotaxis, positioning, and cell-cell interaction of leukocytes within inflamed tissues (*35*). Factors including lipids, cytokines, and homing receptors (HRs) incorporating chemokine receptors (*3*) controlling migratory patterns of ILC2s in the BM, spleen, gut, mesenteric lymph nodes (*36*), and skin (*37*, *38*) have been identified. Lung ILC2s express high levels of β_1 and β_2 integrins and use β_2 integrins selectively to migrate from the BM to the lung after intranasal allergen [*Alternaria alternata* (Alt)] challenge (*39*). Organ-specific imprinting confers differential gene expression patterns on tissue-resident pulmonary ILC2s (*40*). However, ILC2 motility within the lung during inflammation remains unstudied, and little is known regarding the signals that might regulate it. Studies investigating T cell motility in the lung have described a combination of cell-intrinsic signals and physical guidance cues coupled with biochemical signals provided by the microenvironment in driving cell movement (*41*). However, the environmental guidance signals controlling ILC2 dynamic behavior in the lung remain poorly defined. Here, using IL-13–enhanced green fluorescent protein (eGFP) mice (*28*), combined with several imaging approaches, including lung intravital microscopy, we have documented that ILC2s exhibit amoeboid-like movement in the peribronchial and perivascular space after IL-33–induced lung inflammation. We identified specific molecules that communicate between the inflamed pulmonary environment and ILC2s, uncovering the major environmental factors from which ILC2s interpret locomotory cues within the lung.

RESULTS

The number of ILC2s rapidly increases in the peribronchial and perivascular region after recombinant IL-33 treatment

Under homeostatic conditions, ILC2s exist in relatively low numbers in the lung but are rapidly enriched after recombinant IL-33 (rIL-33)– or rIL-25–induced inflammation (*20*–*24*, *39*), promoting tissue repair during inflammation and regulating immune homeostasis. In this respect, ILC2s are thought to occupy a specific niche in the lung in keeping with their putative role as tissue-resident sentinel cells (*14*). However, whether this locational niche is shared with $CD4^+$ T cells remains unknown. Using *IL13-eGFP* mice, we investigated ILC2 numbers in various sites in the lung both at homeostasis and after acute exposure to either the fungal allergen Alt or rIL-33. We first quantified GFP^+CD45^+ cells among live lymphocytes that were either lineage-positive or lineage-negative cells (fig. S1A). ILC2s were further defined by pregating on live (determined using a fixable LIVE/DEAD dye), $GFP^+CD3^-NKp46^-$ cells that were lineage-negative cells [β T cell receptor (TCRβ), TCRγδ, CD5, CD19, CD11b, CD11c, Fc epsilon RI (FCεR1), granulocyte receptor-1 (GR-1), F4/80, and TER-119] and coexpressed CD90.2, killer-cell lectin like receptor G1 (KLRG-1), CD127, and intracellular cytokine IL-13 (fig. S1B). As expected, in control mice, ILC2s were present in very low numbers in the airways, lung tissue, and lung-draining lymph nodes (mediastinal lymph node; Fig. 1, A to C), as well as the blood, BM, spleen, inguinal, and mesenteric lymph nodes (fig. S2). However, during inflammation induced by intranasal administration of rIL-33 or Alt, ILC2 numbers significantly increased in the bronchoalveolar lavage (BAL) fluid (Fig. 1A), lung tissue (Fig. 1B), and the lung-draining lymph nodes (Fig. 1C), as well as after rIL-33 treatment in the blood and BM but not in the spleen, inguinal, and mesenteric lymph nodes (fig. S2). To confirm that we were not excluding unstimulated ILC2s ($IL\text{-}13^-/GFP^-$) in our gating, we additionally reevaluated ILC2 numbers by gating on $CD45^+lin^-NKp46^-CD3^-$ cells and analyzed the frequency of $GATA\text{-}3^+$ (a faithful transcription factor to define all ILC2s) cells (fig. S3A). Here, we used BALB/c mice instead of IL-13–eGFP mice because the GFP signal was significantly lost after intranuclear staining for GATA-3. BALB/c mice were challenged with phosphate-buffered saline (PBS), Alt, or rIL-33, and lungs, BAL, and blood ILC2s were evaluated by gating on $GATA\text{-}3^+$ ILC2s. Our data suggest that ILC2s in mock-treated mice are still very low in frequency compared with Alt and rIL-33 treatment (fig. S3, B and C) and expressed significantly lower IL-13 and IL-5 (fig. S3D). Furthermore, by phenotyping $GATA\text{-}3^+$ ILC2s for extracellular markers, our data suggest that each of the surface markers is altered as per the type of treatment as shown by the percent expression of each marker (fig. S3, E to H), further highlighting the plasticity of ILC2s in inflammation.

Similarly, imaging precision-cut lung slices (PCLSs) from rIL-33–treated IL-13-eGFP mice revealed substantially more $IL\text{-}13^+GFP^+$ cells (fig. S4A), which largely accumulated around large airways and large blood vessels and, to a lesser extent, around alveolar tissue (fig. S4B). To establish that the $IL\text{-}13^+GFP^+$ cells observed after rIL-33 treatment were predominantly ILC2s, we evaluated the proportion of GFP^+ cells that were $CD45^+lin^-CD4^-$, expressed ILC2-defining markers (CD90.2, CD127, KLRG1, and CD25), and coexpressed intracellular IL-13. Our data showed that 98.86% of observed GFP^+ cells were ILC2s, and only 1.14% of GFP^+ cells were $CD4^-$ T cells (fig. S4C). The source of IL-13 by ILC2s versus $CD4^+$ T cells after 1 week of rIL-33 administration was further quantified (fig. S4D).

Because a minor proportion of $CD4^+$ T cells produced IL-13 in our lung inflammation model, we included a $CD4^-$ T cell antibody (Ab) to precisely evaluate the effects of rIL-33 administration on numbers and phenotype of $CD4^-GFP^+$ ILC2s in PCLS studies. Our PCLS imaging revealed that rIL-33 treatment induced a significant increase in GFP^+ ILC2 numbers compared with Alt- or mock-treated mice (Fig. 1D). rIL-33 treatment induced a sixfold greater ILC2 number compared with Alt treatment (Fig. 1, D and E), consistent with the number of ILC2s detected by flow cytometry (Fig. 1, A to C) and with a shared locational distribution in the inflamed lung tissue (fig. S4A). GFP^+ cells surrounding the bronchioles were significantly greater than the GFP^+ cells in the alveolar tissue (fig. S4B). Most of the GFP^+ cells were IL-13–producing ILC2s (fig. S4, C and D) and hence represented $IL\text{-}13^+$–activated ILC2s, referred from here on as ILC2s for simplicity. Higher-magnification views of the peribronchial space bordering the airways revealed an intimate association of some ILC2s with the airway epithelium and that ILC2s shared a locational niche with $CD4^+$ T cells (Fig. 1F, depicting two representative images from a lung slice). Overall, we demonstrate that rIL-33 treatment significantly increased the number of lung ILC2s compared with Alt or PBS treatment and ILC2s accumulate around the airways of inflamed lungs.

IL-33 stimulation induces ILC2 motility around blood vessels and airways

Intranasal administration of either rIL-33 or Alt induces robust inflammation in the lung (*42*, *43*). A hallmark of acute tissue inflammation is leukocyte recruitment. ILC2s are relatively rare in the lung compared with other leukocytes under homeostatic conditions but accumulate rapidly after rIL-33–induced inflammation (Fig. 1). We have previously

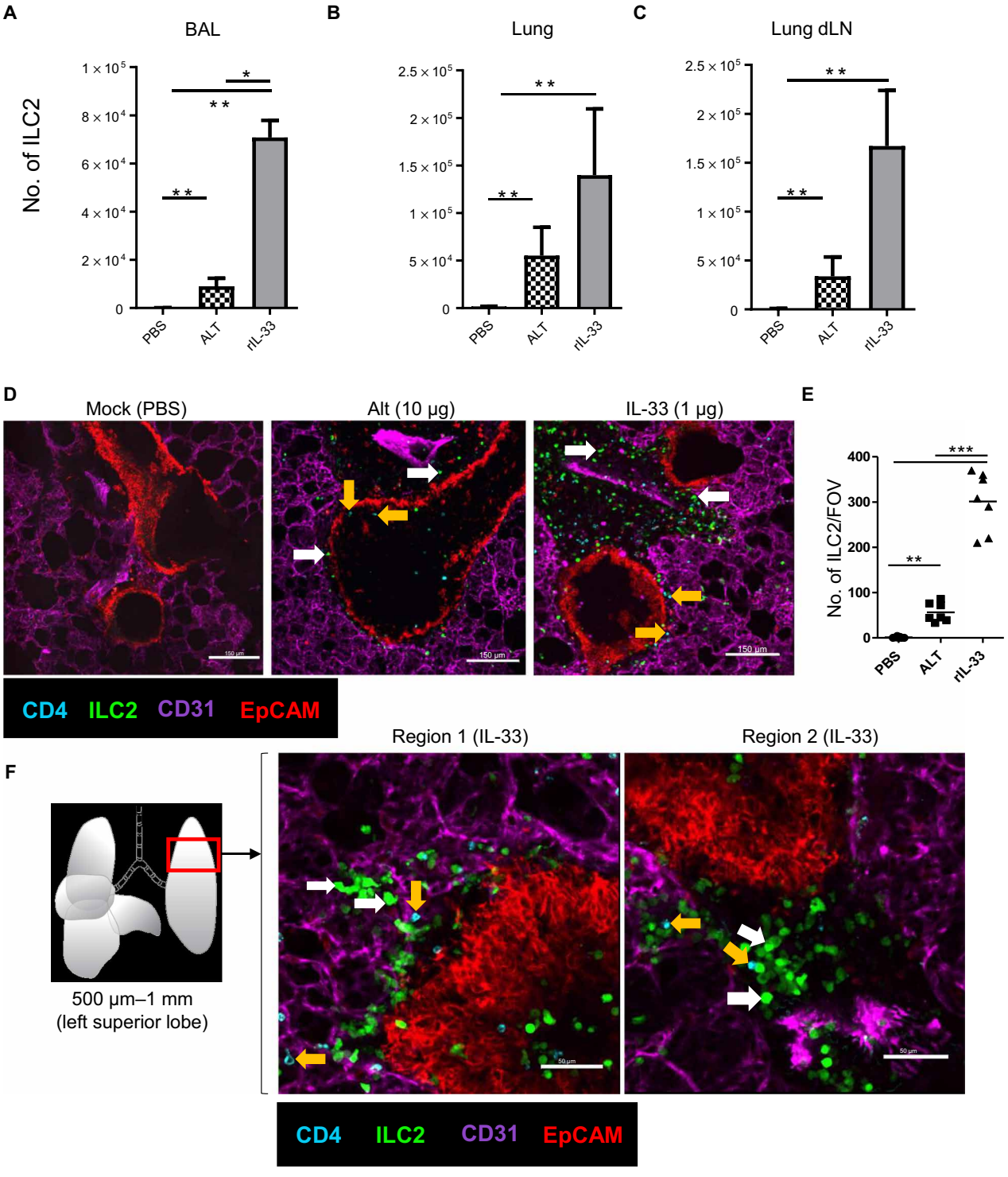

Fig. 1. The number of ILC2s rapidly increases in the peribronchial and perivascular region after rIL-33 treatment. IL-13–eGFP mice were treated with three doses of rIL-33 (1 µg per dose), Alt (10 µg), or PBS (25 µl) over 1 week and culled 24 hours after the final dose. The frequency of ILC2s ($GFP^+CD45^+Lin^-CD3^-NKp46^-CD127^+CD90.2^+KLRG1^+CD25^{var}IL\text{-}13^+IL\text{-}5^+$) in the (**A**) airways (BAL fluid), (**B**) lung, and (**C**) lung-draining lymph nodes (lung dLN; mediastinal). Live viable PCLSs of 200-µm thickness were obtained and stained for CD31 (magenta; the lung structure and blood vessels), CD4 (cyan; T cells, orange arrow), EpCAM (red; to visualize bronchial epithelium), and GFP (ILC2s, white arrow). Images of 1024 µm by 1024 µm field of view (FOV) were taken under a 20× objective using an inverted confocal microscope. (**D**) Images showing ILC2 (GFP^+CD4^-) $CD4^+$ T cells ($CD4^+GFP^-$) location in PBS-, rIL-33–, and Alt-treated mice. Scale bars, 150 µm. (**E**) Number of ILC2s (GFP^+CD4^-) in lung sections per FOV taken under a 10× objective. (**F**) Schematic illustration of the lung depicting the anatomical location in the lung where PCLSs were prepared. Representative images show two regions of the lung slice from a rIL-33–treated mouse showing distribution of ILC2s and $CD4^+$ T cells. Scale bars, 50 µm. $n = 4$ mice per group [mock (PBS)], $n = 6$ mice per group (Alt or rIL-33 treatment). Data are representative of four experiments. $^*P < 0.05$, $^{**}P < 0.01$, and $^{***}P < 0.001$.

demonstrated that the epithelial cell–derived TGF-β induced after rIL-33 treatment promoted a high degree of ILC2 motility in vitro (*34*).

However, to date, dynamic movement of ILC2s has not been visualized in the lung. Because lung ILC2s are relatively rare at homeostasis (Fig. 1, B, D, and E, and fig. S3), we evaluated ILC2 movement in the inflamed lungs of *IL13-eGFP* mice. Imaging live PCLSs from rIL-33–treated *IL13-eGFP* mice showed that ILC2s were motile in the peribronchial and perivascular space (Fig. 2A and movie S1). Closer examination of the lung tissue surrounding the blood vessel revealed that most of the ILC2s exhibited "amoeboid-like" exploratory movement (Fig. 2, B and C, and movies S2 and S3A) with pseudopodia and bleb-like processes in the extravascular lung tissue surrounding the blood vessel, whereas a lesser proportion of ILC2s exhibited "oscillatory" blebbing activity with little actual movement away from their start position (Fig. 2, B and C, and movies S2 and S3B). Similar to oscillatory ILC2s, $CD4^+$ T cells (cyan) did not appear to displace from their point of origin in the lung tissue (Fig. 2B and movie S2). Cell tracking of ILC2s and $CD4^+$ T cells (Fig. 2, D and E) revealed that, in PCLSs from rIL-33–treated mice, ILC2 track speed (Fig. 2F), track length (Fig. 2G), and track displacement (Fig. 2H) were significantly higher than that of $CD4^+$ T cells. ILC2s from Alt-treated mouse lungs moved more slowly, with shorter tracks, compared with rIL-33–treated mice (Fig. 3, A and B). In addition, rIL-33 treatment induced increased ILC2 track speed (Fig. 3C), track length (Fig. 3D), and track displacement (Fig. 3E) compared with Alt treatment. Because rIL-33 promoted greater ILC2 movement than Alt treatment, we focused on rIL-33–induced changes on ILC2 motility thereafter. Because PCLSs do not recapitulate the forces exerted by blood flow and breathing in vivo, we also performed lung intravital microscopy in live mice using a similar strategy to previous work (*44*). We found that consistent with our data in live PCLSs (Figs. 1, D to F, and 2, A and B), ILC2s were enriched in the extravascular tissue close to larger blood vessels and exhibited amoeboid-like movement within the lung tissue (Fig. 3F and movies S4, A and B). In summary, our results demonstrate that ILC2s are highly dynamic after treatment with rIL-33, where they exhibit amoeboid-like movement and travel faster over greater distances than $CD4^+$ T cells.

ILC2s use distinct chemotactic pathways to home to inflammatory sites in the lung

We have shown that, within the lung, ILC2s display a specific distribution pattern and movement behavior distinct from T cells. However, the factors that regulate ILC2 dynamics are not well understood. Because ILC subsets have key features analogous to T cell populations, it has been suggested that molecular pathways, which control motility, migration, and tissue homing, are common to ILC subsets and T cells, but this has not yet been proven. Therefore, we examined the pattern of chemokine receptor expression on ILC populations (defined as $CD45^+GFP^+Lin^-KLRG1^+CD127^+CD25^{var}$) isolated from the lungs of rIL-33–treated mice (or PBS-treated controls; fig. S5, A and B). Unexpectedly, despite the high degree of resemblance between ILCs and T cells, many of the prototypic chemokine receptors found on T cell subsets were absent on ILCs, including CCR3, CCR4 (T_H2), CCR6 (T_H17), and CCR5 and CXCR3 (T_H1). ILCs did express both CCR1 and CCR8, which are associated with type 2 cytokine production by T cells in allergic contexts (*45*).

Therefore, we examined the expression of CCR1, CCR4, and CCR8 specifically on IL-13^+ ILC2s, finding that most of IL-13^+ ILC2s express CCR1 (>50%) and/or CCR8 (>90%) and that the expression of these chemokine receptors was higher in rIL-33–treated mice than in PBS-treated controls (Fig. 4A). In contrast to T cells, we found that CCR4 expression was not associated with a type 2 phenotype in ILCs with only 10% of IL-13^+ ILCs also expressing CCR4. Furthermore, in vivo activation of ILC2s with rIL-33 did not alter CCR4 expression (Fig. 4A). We also found significantly greater levels of CCL8 protein, a ligand for CCR8 in mice (*46*) in the airways (Fig. 4B) and lungs (Fig. 4C) of rIL-33–treated mice compared with PBS-treated control mice. We additionally evaluated other CCR8 ligands (CCL1) and CCR1 ligands (RANTES; fig. S5, C and D) in the lungs of mice exposed to rIL-33 compared with PBS-treated control mice. PCLS and intravital imaging demonstrated that ILC2s accumulate in the peribronchial and perivascular space and are highly motile in rIL-33–treated IL-13–eGFP mice (Fig. 2, A to C, and Fig. 3F). Hence, we determined whether we could identify CCL8 chemokine deposits in areas of ILC2 movement in live PCLSs of rIL-33–treated IL-13–eGFP mice. CCL8 was strongly expressed in the peribronchial space where ILC2s accumulate after rIL-33 treatment, at significantly greater levels than basal CCL8 expression in control mice (Fig. 4, D and E) with airway macrophages being the major producer for CCL8 in our model (fig. S5E).

To examine the migration of ILC2s to chemotactic agents, we sorted human ILC2s from peripheral blood ($CD45^+$, Lin^-, $CD161^+$, $CD127^+$, $CRTH2^+$, and C-Kit^{var}) then cultured with rIL-2, rIL-7, and rIL-33 for at least 4 weeks (resulting in >99% ILC2s). These ILC2s expressed GATA-3 and IL-13 (fig. S6A) and produced IL-13 (fig. S6B). Among the three cytokines required for ILC2 maintenance, our results suggest that IL-7 signaling in ILC2s was critical for their survival, proliferation, and cytokine production as demonstrated by viability (fig. S6C), GATA-3 expression (fig. S6D), Ki-67 staining (fig. S6E), and IL-5 production (fig. S6F). We additionally compared differences in motility between ILC2s starved of IL-2 and IL-33 compared with ILC2s that received all three cytokines. After 12 hours of live ex vivo imaging, ILC2 track speed (fig. S6G) remained comparable (movie S5, A to C). ILC2s that were starved of IL-7 could not be included in this setup because absence of IL-7 significantly reduced ILC2 viability (fig. S6C). Our findings are consistent with the literature and reemphasize the importance of IL-7 signaling being critical for the maintenance of ILC2s and other IL-$7R^+$ lymphocyte populations (*47*).

The potential of in vitro cultured ILC2s to migrate to a known ILC2 chemotactic factor—the eicosanoid PGD_2 (*48*)—was examined using a modified Boyden chamber chemotaxis assay (Fig. 4F). As expected, all human ILC2 lines tested migrated to PGD_2, and peak chemotaxis occurred at a concentration of 100 nM PGD_2 consistent with previous studies (*48*). Because we found CCL8 in the BAL and CCL8 deposits in the lung of rIL-33–treated mice (Fig. 4, D and E), we queried whether CCL8 could induce the migration of human ILC2s. Using the same modified Boyden chamber assay, we found that CCL8 also induced human ILC2 chemotaxis in a dose-dependent manner, peaking at 10 nM CCL8 (Fig. 4G). We next compared migration of ILC2s with factors thought to influence ILC2 movement. After determining the optimum concentrations for each factor, we found that although PGD_2 was the most efficacious inducer of ILC2 migration, TGF-β, IL-33, and CCL8, all promoted comparable levels of migration (Fig. 4H). Together, these data identify specific chemokine receptor expression in ILC2s and show the corresponding ligand availability in areas of ILC2 accumulation. To confirm that

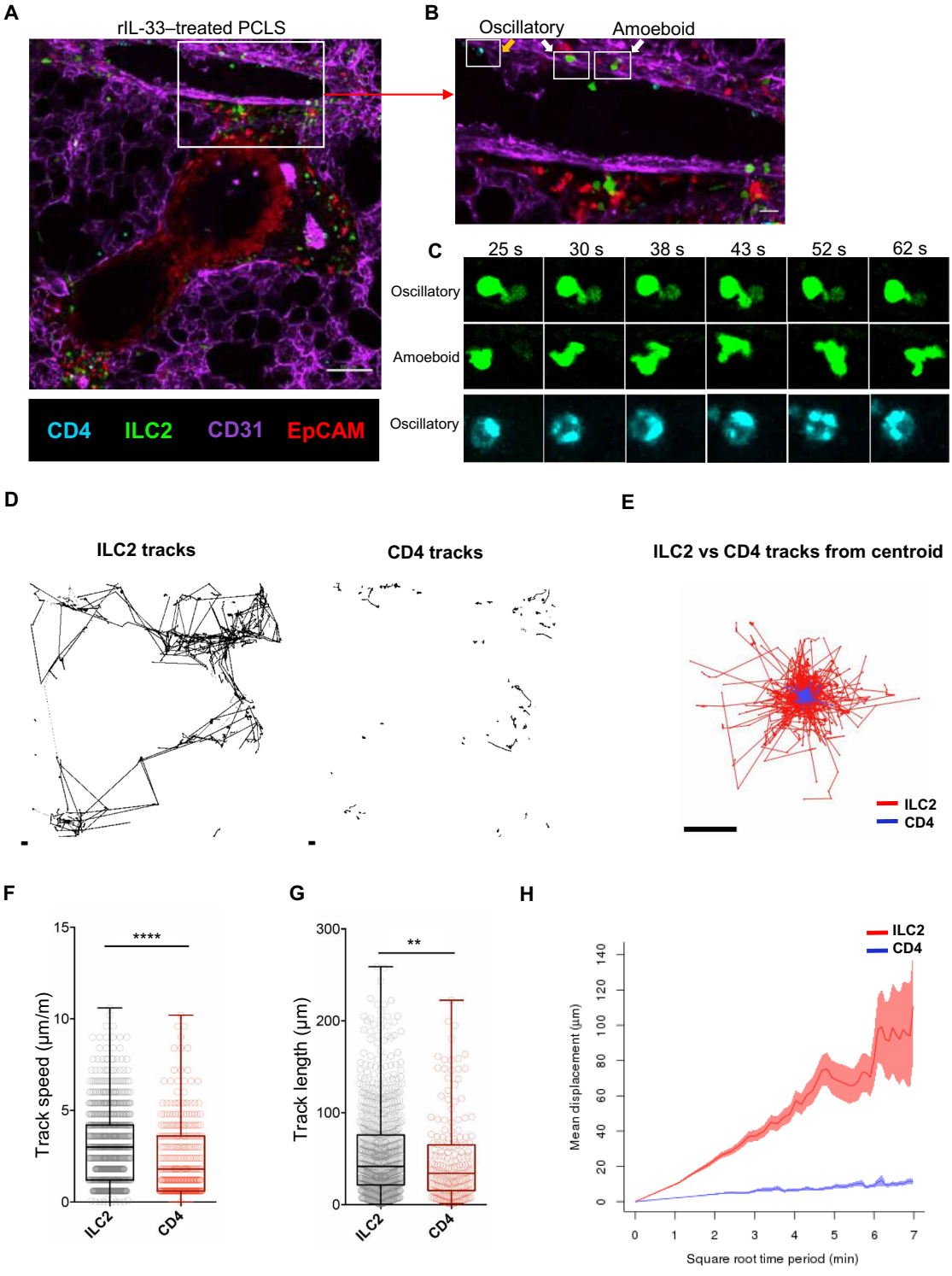

Fig. 2. rIL-33 stimulation induces ILC2 motility around blood vessels and airways. IL-13–eGFP mice were treated with three doses of rIL-33 (1 μg per dose) over 1 week and culled 24 hours after the final dose. Live viable PCLSs of 200-μm thickness were obtained and stained for CD31 (magenta; the lung structure and blood vessels), CD4 (cyan; T cells, orange arrow), EpCAM (red; to visualize bronchial epithelium), and GFP (ILC2s, white arrow), and time-lapse video was taken (1024 μm by 1024 μm FOV, 45-min duration under a 20× objective using an inverted confocal microscope). (**A**) Static image depicting the location of ILC2s and CD4$^+$ T cells. Scale bar, 100 μm. (**B**) Zoomed in section of the blood vessel in (A). Scale bar, 20 μm. (**C**) High-power images of boxed cells in (B) showing differences in pattern of cell movement (oscillatory versus amoeboid movement). ILC2s and CD4$^+$ T cells dynamics were tracked and plotted as (**D**) individual tracks or (**E**) tracks commencing from centroid and overlaid. (**F**) Track speed, (**G**) track length, and (**H**) track displacement were quantified. Representative images shown in (A) to (C) are from rIL-33–treated mice, where $n = 6$ mice per treatment (three slices per mouse were imaged). For (F) to (H) in box and whiskers plots, each dot represents an individual cell. Data are representative of four experiments, where $n = 6$ mice per treatment. $^{**}P < 0.01$ and $^{****}P < 0.0001$.

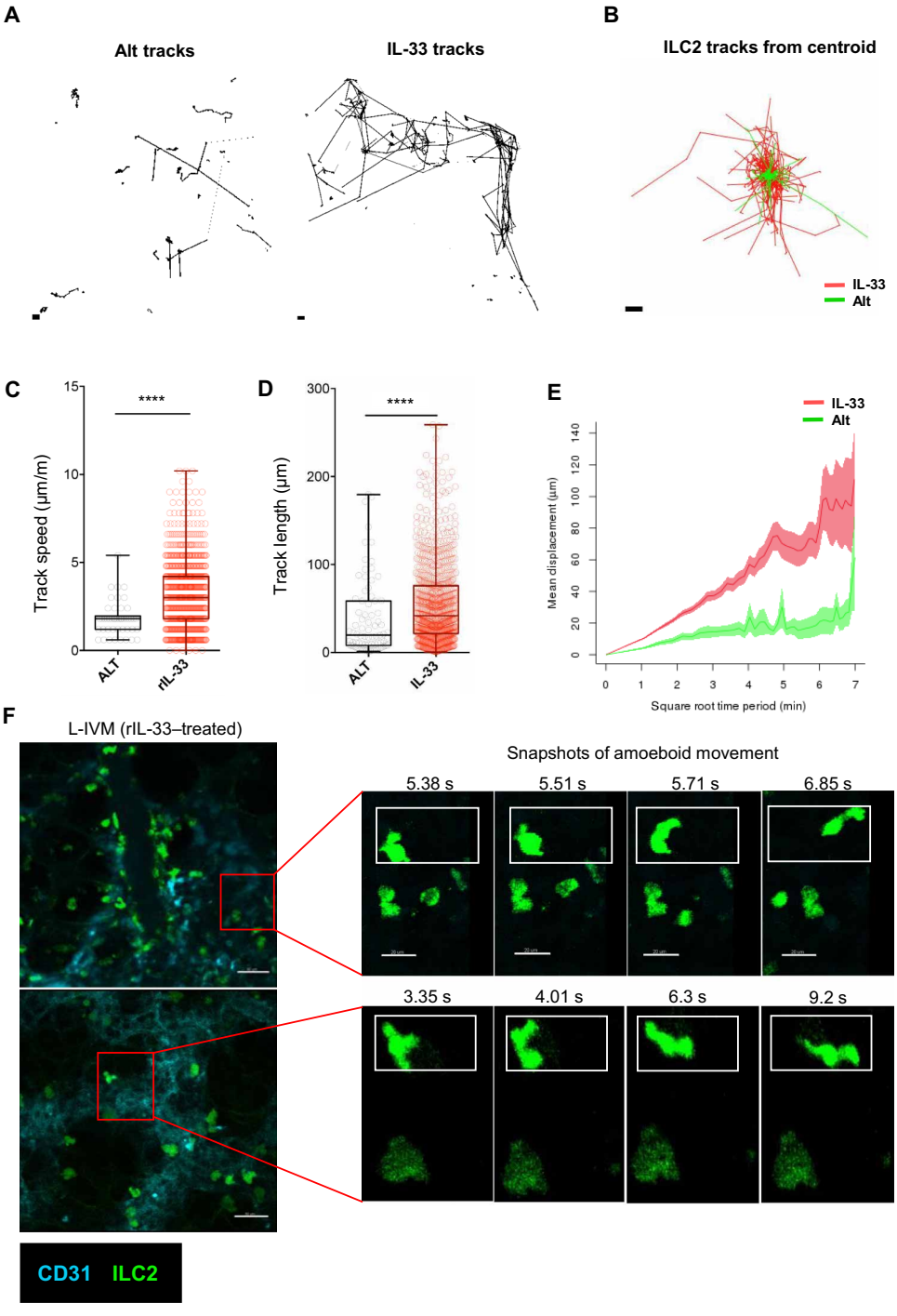

Fig. 3. rIL-33 stimulation induces ILC2 motility around blood vessels and airways. IL-13–eGFP mice were treated with three doses of rIL-33 (1 μg per dose) or Alt (10 μg) over 1 week. Live PCLSs were obtained, ILC2 dynamics were compared between the two, and the differences were plotted as (**A**) individual tracks and (**B**) tracks commencing from centroid and overlaid. Differences in tracks between treatments were quantified as (**C**) track speed, (**D**) track length, and (**E**) track displacement. Intravital microscopy (IVM) was performed in live IL-13–eGFP mice after rIL-33 treatment (one 512 μm by 512 μm FOV in a 1-hour-duration video). (**F**) Static images of different frames captured during the course of the video depicting amoeboid shape changes of ILC2s at separate time points. Scale bars, 20 μm. $n \geq 4$ mice per group. Data are representative from four experiments. ****$P < 0.0001$. Quantifications from (A) to (E) are representative of four experiments, where $n = 6$ mice per treatment (three slices per mouse were imaged). For (F), intravital microscopy images are representative of six individual IL-33–treated mice.

CCL8-CCR8 axis plays an important functional role in ILC2 migration in vivo, we administered a blocking Ab against CCR8 or isotype Ab as a control and simultaneously treated mice with rIL-33. Our live PCLS data showed that blocking CCR8 significantly reduced ILC2 accumulation in the peribronchial region compared with control mice (Fig. 4, I and J), and ILC2 migration was impaired after CCR8 receptor blocking (movie S6, A and B) with shorter tracks depicted as track overlay between treatments (Fig. 4K) and reduced track length (Fig. 4L), track speed (Fig. 4M), and track displacement (Fig. 4N). Closer analysis of ILC2s from each of these treatments revealed that significantly less of the ILC2s in rIL-33–treated mice receiving the anti-CCR8 blocking Ab expressed IL-13$^+$IL-5$^+$ (Fig. 4O), and those cells that did express the type 2 cytokines had significantly less IL-13 and IL-5 as determined by the mean fluorescence intensity (MFI; Fig. 4, P to R). Overall, our data suggest that the CCL8-CCR8 pathway plays an essential role in inducing ILC2 accumulation, activation, and movement within the lung during rIL-33–induced inflammation.

Extracellular matrix proteins, collagen-I, collagen-IV, and fibronectin promote increased ILC2 motility

In addition to chemokines, structural guidance cues such as extracellular matrix (ECM) proteins have been shown to facilitate movement of immune cells, including T cells (*41*). In chronically inflamed lung tissue, as observed during asthma, aberrant ECM expression from tissue remodeling can further influence immune cell activation and survival, thereby altering inflammatory immune responses (*49*). Therefore, we next examined whether ECM proteins influenced ILC2 movement. Fibronectin, collagen-I, collagen-III (fibrillar collagens), and collagen-IV (basement membrane collagen) are located around large airways and blood vessels and are altered during lung inflammation (*50*). Proteoglycans such as versican and tenascin C are changed during remodeling in various lung disorders, including asthma and chronic obstructive pulmonary disease (*51*).

Therefore, the influence of collagen-I, collagen-III, collagen-IV, fibronectin, and proteoglycans, versican and tenascin C,

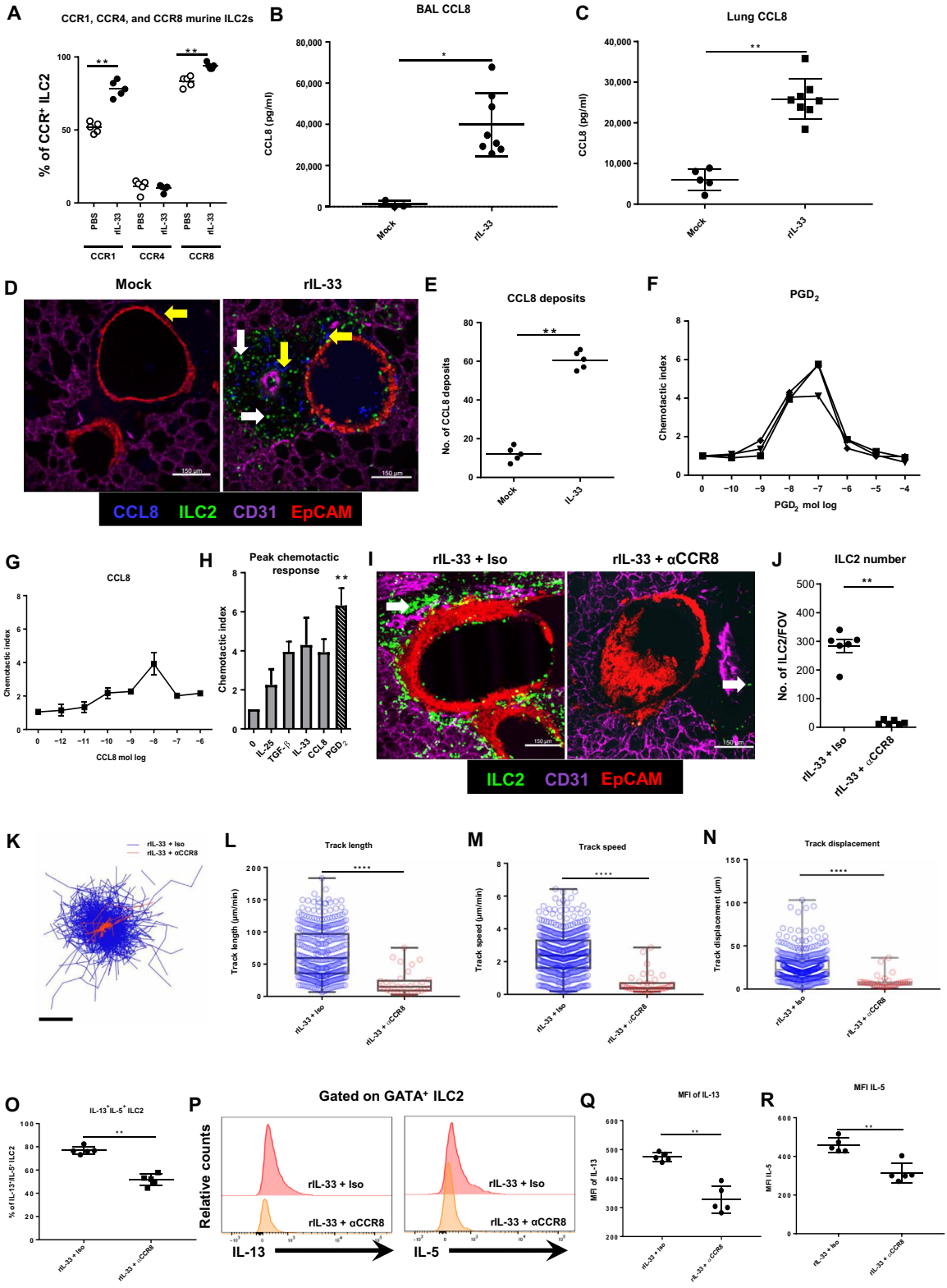

Fig. 4. ILC2s use distinct chemotactic pathways to home to inflammatory sites in the lung. IL-13–eGFP mice were treated with three doses of rIL-33 (1 μg per dose) or PBS (25 μl) over 1 week and culled 24 hours after the final dose. (**A**) The percentage of murine ILC2s ($CD45^+Lin^-NKp46^-CD3^-$) expressing CCR1, CCR4, and CCR8. CCL8 levels in murine (**B**) BAL and (**C**) lung. (**D**) Location of CCL8 expression and ILC2s and (**E**) quantified CCL8 deposits in PCLSs stained for CD31 (magenta; the lung structure and blood vessels), CCL8 (cyan; yellow arrow), EpCAM (red; to visualize bronchial epithelium), and GFP (ILC2s, white arrow), images of 1024 μm by 1024 μm FOV. Scale bars, 150 μm. Human ILC2 lines were generated, and migration to varying concentrations of (**F**) PGD_2 and (**G**) CCL8 was determined. (**H**) Peak migratory responses of a human ILC2 cell line to IL-25, TGF-β, rIL-33, CCL8, and PGD_2. IL-13–eGFP mice treated with rIL-33 were also treated with 5 μg of purified anti-mouse CCR8 Ab intraperitoneally, rCCL8 intranasally, or an isotype control, and PCLSs were obtained and stained. (**I**) Localization of ILC2s in live PCLSs. (**J**) Number of ILC2s per FOV under 10× objective. Time-lapse imaging of 45 min duration was performed, and ILC2 (**K**) track from centroid, (**L**) track length, (**M**) track speed, and (**N**) track displacement were quantified. In box and whiskers graphs, each data point represents an individual cell. BALB/c mice treated with rIL-33 were further treated with rCCL8, αCCR8, or isotype (Iso) control Ab. (**O**) Percentage of $IL\text{-}13^+IL\text{-}5^+$ ILC2s ($CD45^+lin^-NKp46^-CD3^-GATA\text{-}3^+$). (**P**) Representation histogram of MFI of IL-13 and IL-5 and quantification of MFI for (**Q**) IL-13 and (**R**) IL-5 from $GATA^+$ ILC2s. For (A) to (E), $n \geq 4$ mice per group. Data are representative of four experiments. For (F) to (H), $n = 3$ individual donors. Data are representative of three experiments. For (I) to (R), $n = 5$ mice per group. Data are representative from two experiments. $^*P < 0.05$, $^{**}P < 0.01$, and $^{****}P < 0.0001$.

on ILC2 movement was examined in a simplified two-dimensional (2D) cell migration assay. Human ILC2s were cultured on these substrates, and cell movement was tracked over 12 hours in vitro using an automated live-cell imaging system using culture media with or without heat-inactivated fetal bovine serum (FBS) as controls. In contrast to serum-free media, collagen-I, fibronectin, and collagen-IV significantly enhanced dynamics of ILC2s, as shown in the cell tracks and speeds (Fig. 5, A to C, and movie S7, A to E). As expected, FBS-supplemented media significantly enhanced cell movement (Fig. 5, A to C, and movie S7B). In contrast to collagen-I, fibronectin, and collagen-IV, which showed strong effects on ILC2 dynamics, collagen-III, versican, and tenascin C showed minimal influence on ILC2 movement (fig. S7A). Collagen fibers also produce contrast in two-photon microscopy by generating a strong second harmonic signal in tissue. Second harmonic generation (SHG) imaging suggested that the area around bronchioles and associated vessels had a strong fibrillar collagen component in both IL-33–treated and control PCLSs (Fig. 5D). We noticed a qualitative difference in the SHG signal with the collagen fibers in perivascular/peribroncheal areas of rIL-33–treated mice appearing "spikier" than those in PBS-treated control mice. Therefore, we analyzed the geometry of the SHG images of fibrillar collagen in the perivascular/peribronchial area using a gray-level cooccurrence matrix (GLCM) technique to quantify and compare the SHG signal (*52*, *53*). Initially, we plotted correlation versus comparison distance. This analysis compares the organization of the ECM by considering how far it is possible to travel in a straight line away from a start point and observe the same intensity (gray level) between pairs of pixels. Images containing features that are generally organized in long straight lines will therefore have higher levels of intensity correlation over longer comparison distances, and images that display structures more randomly orientated will lose this correlation at shorter comparison distances producing decays with steeper slopes. As can be seen from the data (Fig. 5E), GLCM SHG analysis of the perivascular/peribronchial area from IL-33–treated mice gave steeper decays than the controls, indicating a more disordered arrangement of shorter fibers. We also plotted homogeneity versus comparison distance. This parameter considers the distribution of gray levels at different comparison distances across the image. Therefore, images that have a texture less consistent with long fibrillar structures will have steeper decays in homogeneity with comparison distance. These data (Fig. 5, D and E) also highlighted contrast between the two conditions.

In addition to collagen, fibronectin expression was also evaluated by staining for fibronectin in live PCLSs from PBS- or rIL-33–treated mice. Our results showed that fibronectin expression is enriched in the peribronchial region of rIL-33–treated mice (Fig. 5F). Collectively, our data indicate that collagen-I, collagen-IV, and fibronectin influence ILC2 speed in vitro. Furthermore, collagen and fibronectin are modified in areas where ILC2s accumulate during rIL-33–induced inflammation.

Collagen-I enhances ILC2 actin cytoskeletal remodeling and polarity

ECM protein "tracks" can define the path of motile cells through the tissue (*54*). We observed that ILC2s exhibited amoeboid-like movement after rIL-33–induced inflammation (Figs. 2 and 3F). Amoeboid cell movement involves the induction of a simple polarized shape, dynamic pseudopod protrusion and retraction, flexible oscillatory shape changes, and rapid low-affinity crawling (*55*). Our results showed that ECM proteins collagen-I, fibronectin, and collagen-IV promoted increased human ILC2 motility in a 2D migration assay. Therefore, we next tested whether each ECM protein directly influenced changes in ILC2 phenotype, cytokine production, and shape change in the same 2D environment. We found that ILC2 GATA-3 expression (fig. S7B) and IL-5 production (fig. S7C) remained comparable after incubation over collagen-I or collagen-IV. However, collagen-I selectively induced the most pronounced ILC2 shape change with characteristically elongated ILC2 cell bodies visible (Fig. 6, A and B). In amoeboid movement, force generation (protrusion and contraction) and force transduction (adhesion) are controlled by actomyosin cytoskeletal remodeling (*56*). We imaged f-actin localization and quantified ILC2 shape after 12 hours on the different ECM. ILC2s seeded on collagen-I were highly polarized with areas of f-actin accumulation (Fig. 6B) and had significantly greater cell area and perimeter (Fig. 6, C and D). Together, these data indicate that collagen-I influences ILC2 shape toward the promigratory exploratory phenotype we described in vivo (Figs. 2 and 3F).

Blocking collagen fibrillogenesis in vivo increases ILC2 dynamics and reduces eosinophil accumulation in the inflamed lung

We have previously demonstrated that epithelial cell–derived TGF-β1, induced after rIL-33 treatment, can drive ILC2 movement (*34*). Furthermore, our results show that collagen-I significantly alters ILC2 shape by elongating the cell body (Fig. 6). TGF-β has been shown to enhance collagen-I and collagen-III mRNA expression during remodeling, and blocking collagen deposition restores baseline collagen levels (*57*). We observed changes to collagen geometry in the peribronchial space where ILC2s are highly dynamic after rIL-33 treatment (Fig. 5, D and E). Hence, we next investigated whether we could extend our findings from the 2D assays previously described in Fig. 6 into in vivo 3D tissue by blocking newly synthesized collagen and measuring ILC2 movement after rIL-33–induced inflammation. The fibrillar structure of collagen-I morphology is stabilized by inter- and intramolecular cross-links initiated by lysyl oxidases whose expression can be inhibited by β-aminopropionitrile (BAPN) (*57*). After rIL-33 treatment, we administered BAPN intraperitoneally. Mice that received rIL-33 along with the collagen cross-linking inhibitor showed longer tracks depicted as individual tracks (Fig. 7A) and track overlay between treatments (Fig. 7B). Cell track quantification revealed that ILC2s from the lungs of mice that were rIL-33–treated along with BAPN displayed increased ILC2 track speed (Fig. 7C), track length (Fig. 7D), and track displacement (Fig. 7E) compared with rIL-33–treated mice suggestive of a reduced interaction with the ECM.

Although addition of BAPN altered ILC2 motility in rIL-33–treated mice, ILC numbers only slightly reduced in the lungs (Fig. 7F) with comparable ILC2 numbers in the BAL (Fig. 7G) and blood (Fig. 7H). We additionally tested whether BAPN directly activated ILC2s by evaluating cytokine production by ex vivo sorted ILC2s from rIL-33–treated IL-13–eGFP mice. Our results showed that, within the time frame of 36 hours after incubation, IL-5 production by ILC2s remained unchanged after incubation with collagen-I + BAPN or collagen-I alone (fig. S8A). Addition of rCCL8 to the cultures significantly increased IL-5 production (fig. S8A). We next evaluated whether blocking collagen fibrillogenesis in rIL-33–treated mice affected on the inflammatory infiltrate in the lungs and altered

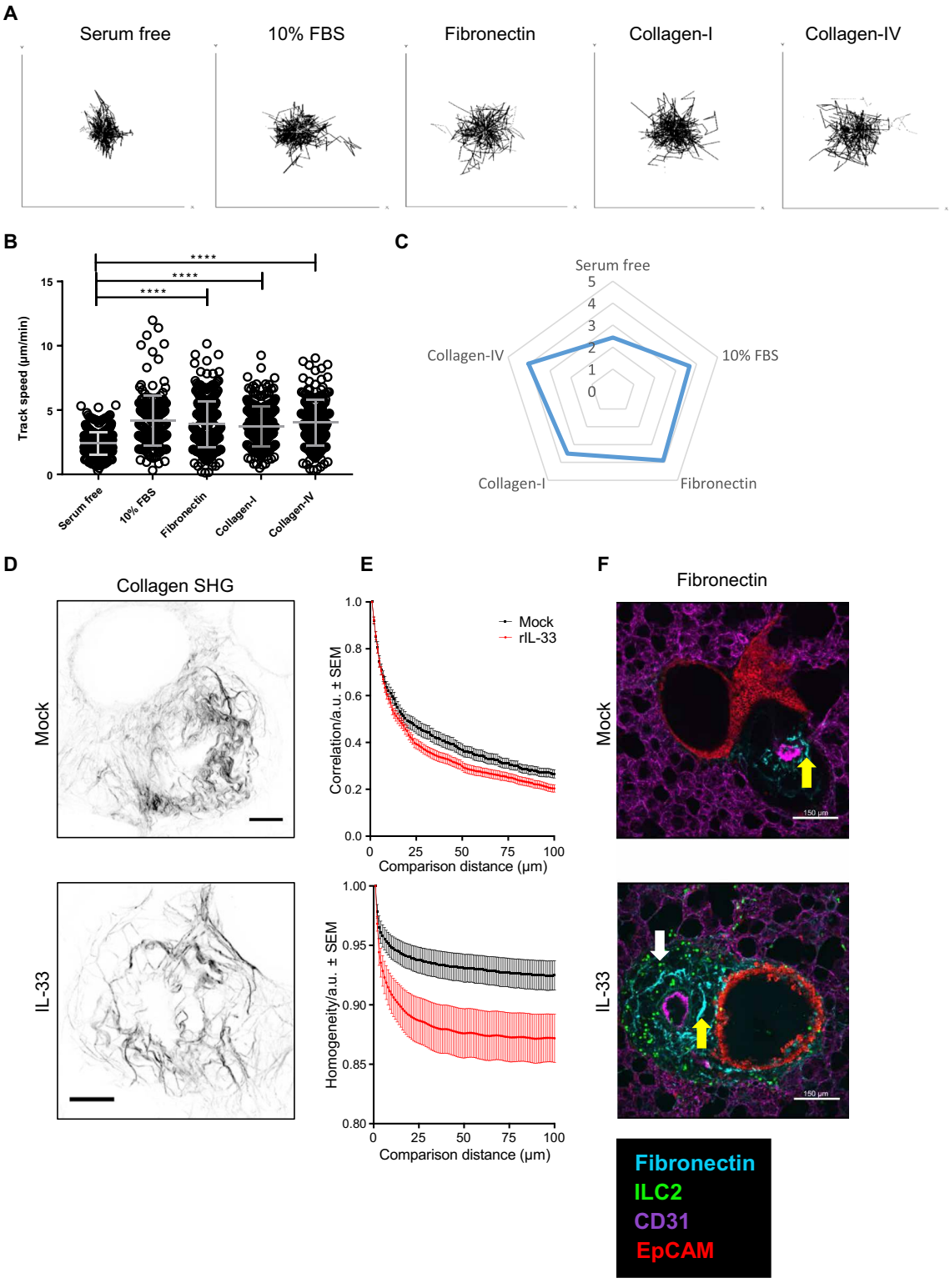

Fig. 5. ECM proteins, collagen-IV, and fibronectin promote increased ILC2 motility. Human ILC2 lines were seeded on tissue culture plates coated with either 10% FBS, fibronectin, collagen-I, collagen-IV, or serum-free coating (control) for 24 hours. Cell movement was imaged via the JuLI imaging system and plotted as (**A**) individual tracks, (**B**) track speed dot plots, and (**C**) track speed spider plots. IL-13–eGFP mice were treated with three doses of rIL-33 (1 μg per dose) or PBS (25 μl) over 1 week and culled 24 hours after the final-dose PCLS was obtained. (**D**) SHG imaging of PCLSs revealing collagen fibers, representative maximum intensity projections. Scale bars, 50 μm. (**E**) GLCM analysis of SHG imaging. a.u., arbitrary units. (**F**) Images of fibronectin expression and localization. PCLS stained for CD31 (magenta; the lung structure and blood vessels), fibronectin (cyan; yellow arrow), EpCAM (red; to visualize bronchial epithelium), and GFP (ILC2s, white arrow), and images of 1024 μm by 1024 μm FOV were taken. Scale bars, 150 μm. For (A) to (C), $n = 3$ donors (in triplicate). Data are representative of three experiments. For (D) to (F), $n = 6$ (in triplicate). ****$P < 0.0001$.

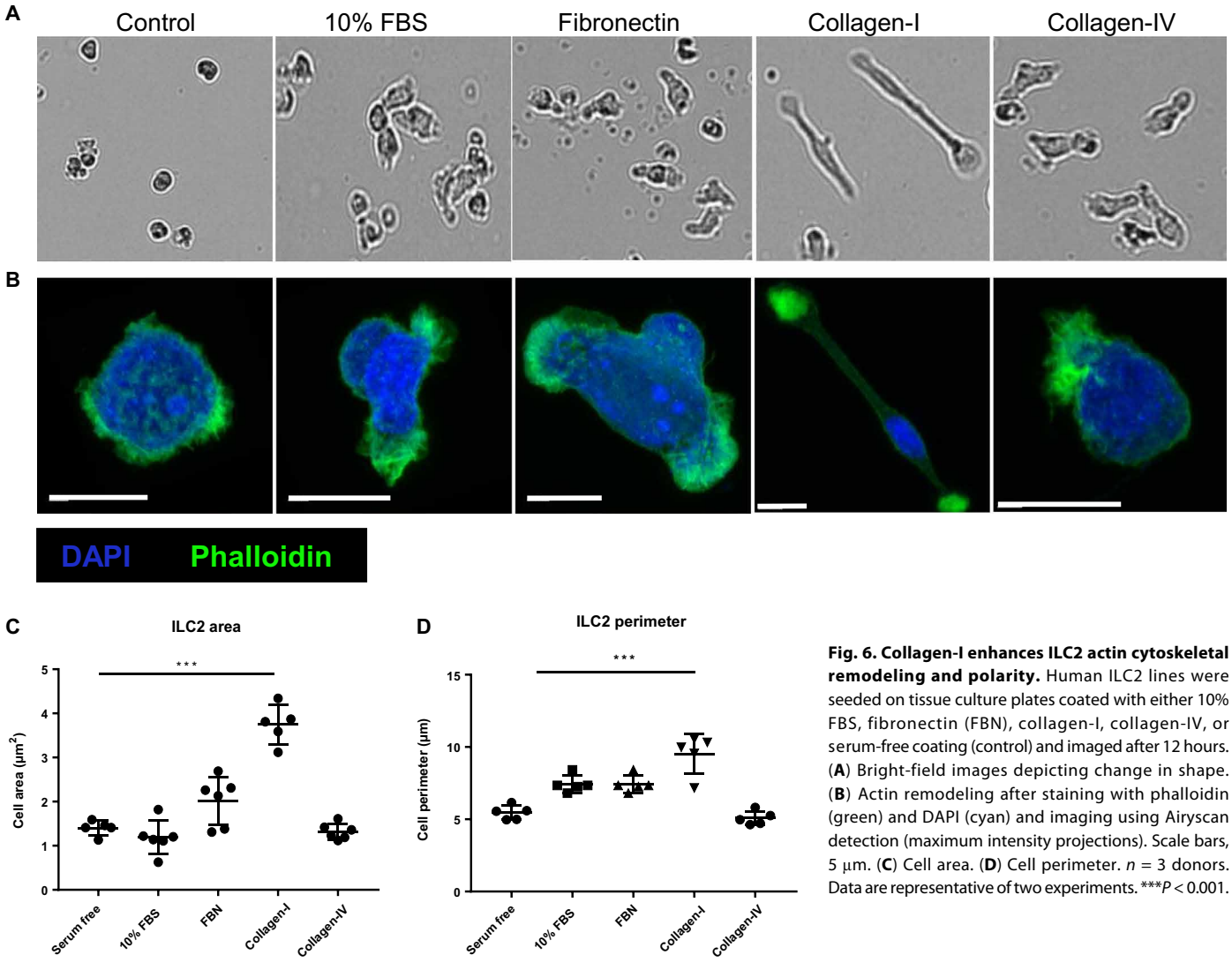

Fig. 6. Collagen-I enhances ILC2 actin cytoskeletal remodeling and polarity. Human ILC2 lines were seeded on tissue culture plates coated with either 10% FBS, fibronectin (FBN), collagen-I, collagen-IV, or serum-free coating (control) and imaged after 12 hours. (**A**) Bright-field images depicting change in shape. (**B**) Actin remodeling after staining with phalloidin (green) and DAPI (cyan) and imaging using Airyscan detection (maximum intensity projections). Scale bars, 5 μm. (**C**) Cell area. (**D**) Cell perimeter. $n = 3$ donors. Data are representative of two experiments. ***$P < 0.001$.

lung function. rIL-33 + BAPN–treated mice had unchanged lung function (Fig. 8A) and comparable numbers of airway macrophages (Fig. 8B), dendritic cells (Fig. 8C), and neutrophils (Fig. 8D) compared with mice treated with rIL-33 alone. Blocking collagen fibrillogenesis in rIL-33–treated mice significantly reduced the frequency of eosinophils (Fig. 8E) and lung CCL24 levels (Fig. 8F), whereas eosinophil motility remained unaltered compared with mice treated with rIL-33 alone (movie S8, A and B) and further quantified by track length (fig. S8B) and track speed (fig. S8C). We lastly compared eosinophil accumulation in the peribronchial region of the lungs where ILC2s accumulate and found significantly lower number of eosinophils as demonstrated by Congo red staining (Fig. 8, G and H).

Therefore, blocking newly synthesized collagen during rIL-33 treatment significantly changed ILC2 motility and the ensuing eosinophil accumulation. These data indicate that ILC2 interactions with the ECM may affect their function and contribution to eosinophilic inflammation.

DISCUSSION

Immune cell recruitment in inflammation involves emigration of activated leukocytes from the vasculature across inflamed endothelium into the tissue space through activation of specific effector programs (*58*). The ensuing response must be robust enough to control infection or repair damage but sufficiently restrained so as to prevent excessive tissue damage and pathology. Mucosal surfaces, such as the lung, constantly encounter potentially harmful threats in the form of microbes, allergens, and pollutants that can damage lung tissue and impair normal physiological lung function. ILC2s are central in orchestrating type 2 immunity (*28*) and promoting tissue repair (*13*). We have previously shown that, during lung inflammation, in vivo and in vitro TGF-β expression influences ILC2 movement, but the mechanisms that promote ILC2 migration are not well understood (*34*). Hence, a more detailed spatiotemporal analysis of ILC2 induction and dynamics in the lung is of great importance to develop a thorough appreciation of ILC2 behavior and function and their interaction with other cells during type 2 inflammatory responses. Because ILC2s are a rare immune cell population in the lung at homeostasis (*28*), visualizing ILC2s by intravital imaging in the lungs of living animals has been challenging. Delivery of rIL-33 in mice drives type 2 immunity, and ILC2s expand robustly and produce large amounts of IL-13 (*28*, *34*) even in the absence of T and B cells (*42*). Here, using a model of rIL-33 or Alt-driven lung

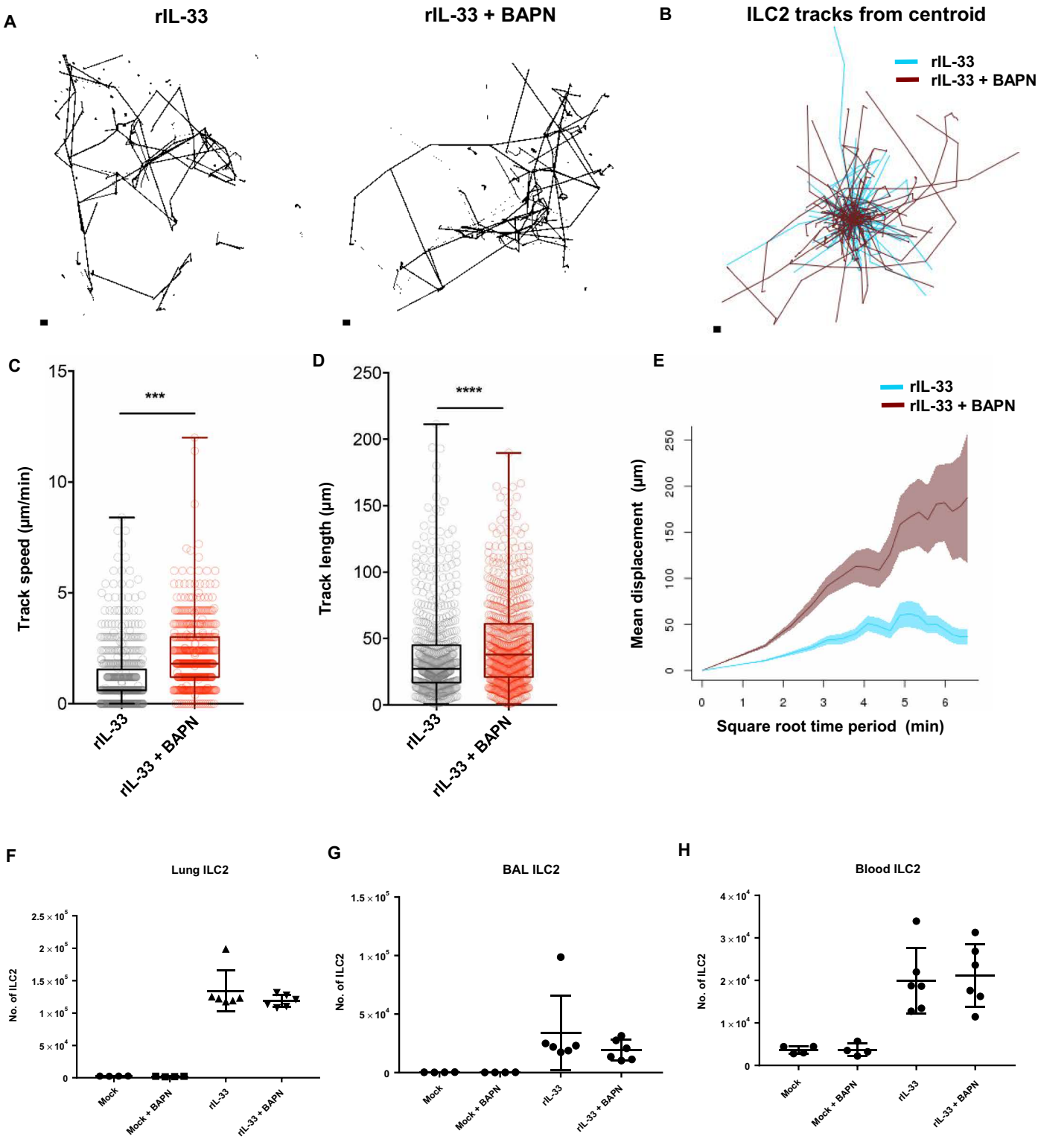

Fig. 7. Blocking collagen fibrillogenesis in vivo increases ILC2 dynamics in the inflamed lung. IL-13–eGFP mice treated with rIL-33 were further treated with BAPN along with controls were culled 24 hours after the final dose. ILC2 dynamics from live PCLSs were plotted as either (**A**) individual tracks or (**B**) tracks commencing from centroid and overlaid. Differences in tracks between treatments were quantified as (**C**) track speed, (**D**) track length, and (**E**) track displacement. Total ILC2s in (**F**) lungs, (**G**) BAL, and (**H**) blood were enumerated. For (A) to (E), $n \geq 4$ mice per group. Data are representative from four experiments. For (F) to (H), $n = 6$ mice per group. Data are representative from two experiments. ***$P < 0.001$ and ****$P < 0.0001$.

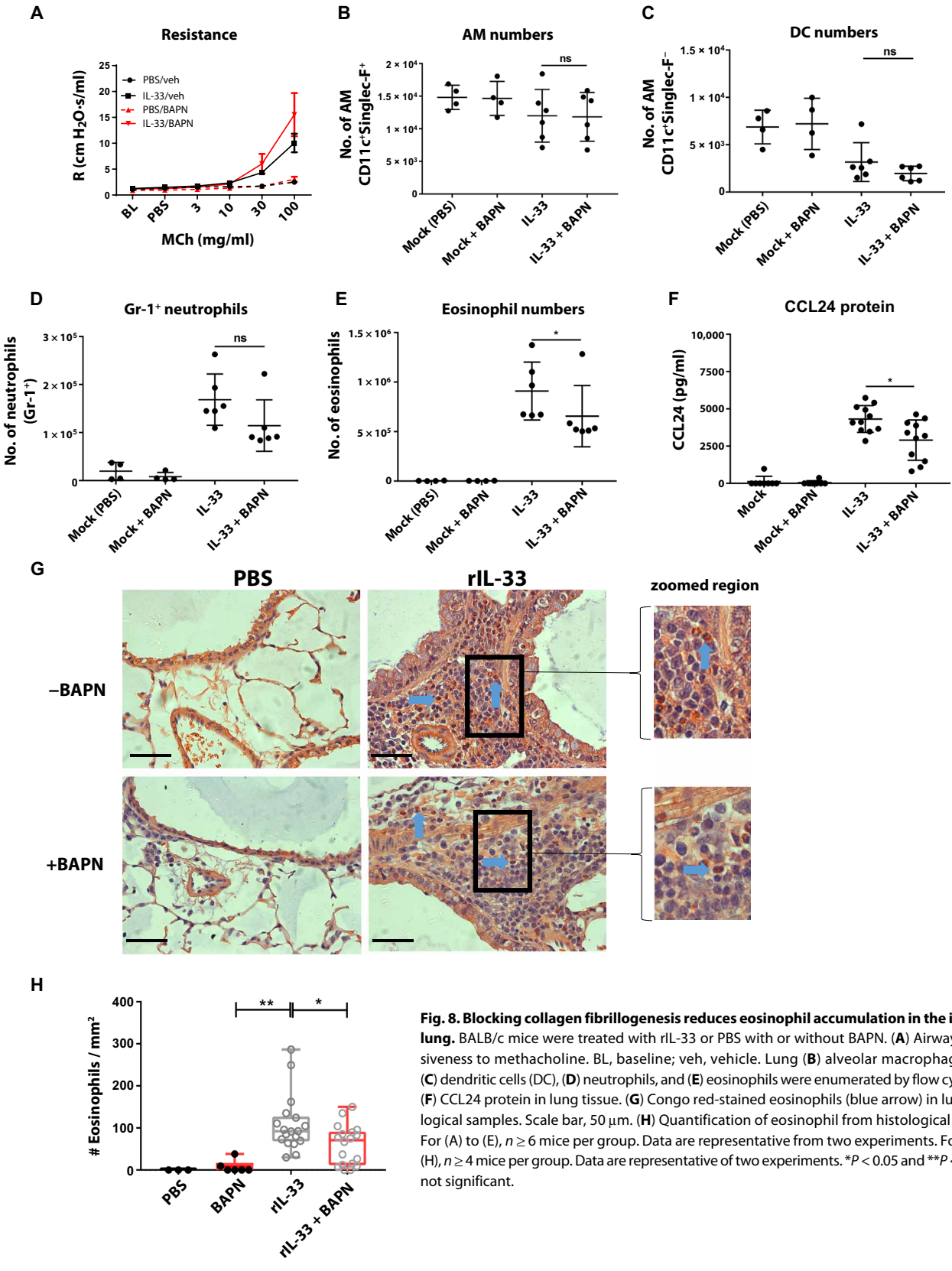

Fig. 8. Blocking collagen fibrillogenesis reduces eosinophil accumulation in the inflamed lung. BALB/c mice were treated with rIL-33 or PBS with or without BAPN. (**A**) Airway responsiveness to methacholine. BL, baseline; veh, vehicle. Lung (**B**) alveolar macrophages (AM), (**C**) dendritic cells (DC), (**D**) neutrophils, and (**E**) eosinophils were enumerated by flow cytometry. (**F**) CCL24 protein in lung tissue. (**G**) Congo red-stained eosinophils (blue arrow) in lung histological samples. Scale bar, 50 μm. (**H**) Quantification of eosinophil from histological samples. For (A) to (E), $n \geq 6$ mice per group. Data are representative from two experiments. For (G) and (H), $n \geq 4$ mice per group. Data are representative of two experiments. *$P < 0.05$ and **$P < 0.01$. ns, not significant.

inflammation in IL-13–eGFP knockin mice, combined with sophisticated lung imaging, we demonstrate that ILC2s are highly dynamic in the lung in vivo. After an acute inflammatory exposure, ILC2 numbers in the lung increased substantially by around 30-fold (Alt) to 100-fold (rIL-33). Simultaneously, our results show an incremental increase in the number of ILC2s in both the lung-draining lymph nodes and circulation after Alt- or rIL-33–induced inflammation. A recent study reported that administration of rIL-33 in mice promotes the egress of ILC2 progenitors (ILC2Ps) from the BM to peripheral tissues, whereas mice lacking IL-33 signaling had a significant accumulation of ILC2Ps in the BM (*59*). This suggests that the rapid expansion in ILC2 numbers induced in the lung in our model of rIL-33 inflammation could result as a consequence of recruitment of ILC2Ps from the BM rather than in situ proliferation of a small steady-state resident precursor. In addition, there was no increase in ILC2 numbers in the spleen or non–lung-draining lymph nodes, indicating that intranasal rIL-33 signals for ILC precursors in the BM to traffic to the lungs. Our imaging studies also depict ILC2 accumulation in the extravascular tissue surrounding large blood vessels, again indicating that these cells are perhaps likely to be recent emigrants from the BM.

In the lung, we found that ILC2s mainly accumulate in the peribronchial and perivascular area and, to a lesser extent, in the parenchyma. The location of ILC2s in the peribronchial area is consistent with their postulated role in promoting epithelial repair. In a previous study, we showed that ILC2s in the airway lumen are primed to respond to epithelial cell–derived TGF-β induced after rIL-33 administration, as a result of high cell surface expression of TGF-βRII, and that epithelial cell–derived TGF-β enhanced the migratory activity of ILC2s (*34*). Hence, a critical molecular communication exists between ILC2s and bronchial epithelial cells to promote ILC2 movement during lung inflammation and could explain why ILC2s home to the peribronchial region of the lung tissue.

By using live lung slices, we demonstrated an amoeboid pattern of movement of lung ILC2s after rIL-33 treatment. This observation was recapitulated in the lungs of live intact mice using lung intravital microscopy of rIL-33–treated IL-13–eGFP mice. We found that, similar to our data in live lung slices, ILC2s were enriched in the lung tissue surrounding larger blood vessels rather than the alveolar capillaries and characteristically move in an amoeboid manner during locomotion. However, despite their functional and phenotypic similarities to $CD4^+$ T cells, ILC2s differed markedly in their migratory behavior, moving faster and to greater distances than $CD4^+$ T cells in the inflamed lung. The physical proximity of motile ILC2s to epithelial cells further supports the notion that ILC2s may directly influence epithelial cell function and vice versa and may not be restricted to communication via secreted cytokines but could result from physical receptor-ligand interactions. It is known that motility patterns and distances traveled by various leukocyte subpopulations differ (*60*). In our study, we find that lung ILC2s exhibit amoeboid pattern of movement traveling distances in the range of 100 to 200 μm perhaps displaying "searching" or "exploratory" behavior, consistent with their sentinel role at mucosal sites (*61*). Together, our data suggest that lung ILC2s may exhibit motility patterns similar to innate immune cells. This is consistent with findings in the skin, where dermal ILC2s patrol their environment with an average speed similar to that of dermal dendritic cells (*38*). This scanning behavior of ILC2s may be suggestive of their need to detect local alarmins or danger signals by damaged epithelial cells in the lung after an inflammatory insult. Furthermore, the migration of lung ILC2s in close association with bronchial epithelial cells seems likely to ensure that factors secreted by the epithelium, such as TGF-β, can rapidly engage the ILC2s. It presumably also ensures that signaling in the reverse direction, from the ILC2s to the epithelial cells, for promoting epithelial repair can take place efficiently.

Factors driving leukocyte motility include the distribution of adhesion molecules on leukocytes, as well as chemotactic signals. It has been well established that lung ILC2s express both β_1 and β_2 integrins at homeostasis and after Alt-induced inflammation (*39*). Furthermore, ILCs share many of the key features analogous to T cell populations, for example, ILC2s and T cells both use the HR CCR7 to actively migrate to lymphoid tissues (*3*). In addition, it has been shown recently that iILC2s, originating from precursors in the intestinal lamina propria, express high levels of CCR9 and use S1P receptors to exit the intestine into the lymph and move to distant sites, such as the lung, where they display effector activity (*15*). Progenitors to iILC2s do not exist in the lung and are not induced after inflammation induced via the intranasal route (*15*). Hence, the chemokine migratory programs of ILC2s generated in the lung after intranasal-instilled mediator-driven inflammation have remained elusive until now, and very little is understood about the process by which ILC2s are attracted to sites of immune insult in the lungs. At homeostasis, we found that CCR8 and CCR1 were expressed by most of murine lung ILC2s, in contrast to other T cell subsets. However, after rIL-33 treatment, the percentage of CCR8 and CCR1 expressing ILC2s further increased.

In addition, TGF-β acts as an ILC2 chemoactivator, enhancing murine ILC2 migration in a nondirectional manner. Furthermore, both PGD_2 and, to a much lesser extent, IL-33 have been shown to be chemotactic for human skin- and blood-derived ILC2s (*48*). We show that in addition to PGD2, CCL8 is chemotactic for ILC2s with nanomolar potency. We found that CCL8 deposits were strongly expressed in the peribronchial space where murine lung ILC2s accumulate. This could be attributed to the CCL8-CCR8 ligand-receptor axis that has been shown to be crucial in localizing pathogenic T_H2 cells to the site of eosinophilic inflammation and in driving the allergic process in the skin (*62*). To further explore this hypothesis, we blocked CCR8 receptor in rIL-33–treated mice and analyzed effects on ILC2 motility. Our data strongly suggest that signaling via CCR8 is critical for ILC2 cytokine (IL-13 and IL-5) production and motility of $IL\text{-}13^+$–activated ILC2s. A variety of resident pulmonary cells secrete CCL8, the CCR8 ligand in mice. We find that lung airway macrophages are the predominant cellular source of CCL8 in rIL-33–treated mice. Our data suggest a previously undescribed model where macrophage-derived CCL8 acts to increase ILC2 accumulation to areas proximal to epithelial cells.

Overall, our results provide insights into the independent and distinct migration pathways that ILC2s use in contrast to T cells. ECM proteins such as collagens are well known to interact with leukocytes by directly binding to cell surface receptors (*63*). In this respect, changes to subepithelial collagen and ECM protein deposition are important pathophysiological components of airway remodeling in T_H2-driven lung inflammation. We find strong fibrillar collagen deposition around bronchioles and associated vessels in both rIL-33–treated and control PCLSs where lung ILC2s accumulate. rIL-33–treated mice showed quantitative differences in both correlation and homogeneity parameters of fibrillar collagen geometry compared with control mice. rIL-33–induced epithelial TGF-β is chemoactive for ILC2s, and administration of TGF-β in mice increases collagen-I

mRNA expression in mouse lungs (*49*, *57*). This suggests that altered collagen distribution as a result of rIL-33–induced inflammation may influence ILC2 migratory programs. In line with this, our in vitro 2D migration assays indicate that collagen-I exclusively alters ILC2 morphology with enhanced cell spread and elongation of cell body. Hence, in vivo, collagen-I fibers may support a more polarized ILC2 morphology, by increasing ILC2 traction, reducing ILC2 speed, and allowing for longer dwell times in specific sites of inflammation in the lung. Cross-links are essential for the mechanical stability of collagen and have been shown to control T cell mobility (*64*). To test the overall contribution of newly synthesized collagen on ILC2 dynamics, we used BAPN to block the formation of new collagen cross-links by inhibiting the enzyme lysyloxidase. Blockade of collagen fibrillogenesis significantly increased ILC2 speed and travel distance after rIL-33 treatment, hence suggesting that reduced collagen stability, resulting as a consequence of blocking new collagen fibrillogenesis, may disrupt a controlled receptor-ligand interaction of ILC2s with collagen-I fibers, increasing overall dynamics of ILC2s. Although collagen-I blocking increased ILC2 movement, rIL-33–induced eosinophilia was significantly reduced in the lungs of these mice. We have previously reported that, after house dust mite treatment in mice, chemoactive epithelial-derived TGF-β is essential for ILC2 activation and critically controls all hallmarks features of allergic responses including airway hyperresponsiveness and eosinophilia (*34*). Inferring from this knowledge, our data suggest that, although the initial cytokine-driven instruction from structural cells initiates ILC2 movement, components of the inflamed lung environment, namely, CCL8-CCR8 signaling and collagen-I, are critical for regulating controlled ILC2 accumulation and dynamics imperative for ensuring robust type 2 inflammation. Hence, although TGF-β serves as a chemokinetic mediator, CCL8 induced after rIL-33 treatment is an important chemotactic signal that mediates ILC2 motility and cytokine production via CCR8 receptor. Furthermore, the difference in interfibrillar geometry of collagen fibrils alters ILC2 migratory patterns, and the dwell time of ILC2s with collagen fibrils is a critical factor toward ILC2 behavior and function in type 2 inflammation. Thus, combined environmental signals from damaged lung tissue act in concert to mechanistically drive ILC2 migratory patterns in the inflamed lung.

ILC2s are defined by the combination of several extracellular and intracellular markers. Here, we used multicolor flow cytometry of cell suspensions from dissociated lung tissue to identify and quantify these cells, but this approach loses spatiotemporal information by definition. Therefore, we used a combination of imaging using IL-13–GFP reporter mice in combination with a handful of markers and dyes and detailed multicolor flow cytometry together to mitigate potential misidentification of the cells. However, in an ideal experiment, we would be able to image tens of markers simultaneously. Newer approaches (e.g., imaging mass cytometry) are starting to address this, but none allows live organism/cell/tissue imaging to directly address the spatiotemporal dynamics of these populations, a significant challenge in the field.

Overall, using highly sophisticated imaging techniques, we reveal how ILC2s migrate within an inflamed tissue and interact with adjacent cells and lung environmental factors during a type 2 inflammatory response. Specifically, we show that lung ILC2s are highly motile in vivo and exhibit an exploratory amoeboid pattern of movement during inflammation. In addition, we identify signature chemokine receptors used by ILC2s to home to inflammatory sites in the lung. Our data provide previously unidentified insights into the mechanism by which diverse lung environmental factors combine to control ILC2 migration and provide direct evidence for collagen-I in exclusively regulating ILC2 shape and polarity, thereby influencing the outcome of an inflammatory response. Imaging these dynamic cellular events in real time in the lungs of living animals has provided an important visual platform that could be used for further interrogation of ILC2s and other immune cell functions in the context of allergen- or pathogen-driven T_H2 inflammation.

MATERIALS AND METHODS

Mice

Adult female IL-13–eGFP mice (a gift from A. N. McKenzie, MRC Laboratory of Molecular Biology, Cambridge) (*28*) were used for experiments between 7 and 10 weeks of age. Mice were housed under specific pathogen–free conditions and given food and water ad libitum. All procedures were conducted in accordance to the institutional guidelines and under the approval of our Home Office project license [granted under the Animals (Scientific Procedures) Act 1986]. Mice were administered 10 μg of Alt extract (Greer Laboratories) in 25 μl of PBS intranasally three times a week for 1 week or PBS alone as controls. Alternatively, carrier-free recombinant murine rIL-33 (1 μg per dose in 25 μl of PBS; eBioscience) or PBS was administered three times a week for 1 week. Mice were culled 24 hours after the final cytokine or allergen dose.

Live PCLSs

Ex vivo cultured PCLSs provided a 3D cell culture model to image ILC2 dynamics within the lung microenvironment and was adapted and modified from a previously described protocol (*65*). Briefly, before slicing, lungs were inflated with a 0.8-ml volume of 2% low-melting agarose (Thermo Fisher Scientific) prepared in PBS. After inflation, lungs were carefully dissected out and placed in Hanks' balanced salt solution containing 2.5% Hepes (Gibco, Life Technologies). The intact left superior lung lobe was excised, and 200-μm transverse sections were prepared from the upper 1-mm region of the left superior lung lobe using a Compresstome VF-300 vibrating microtome (Precisionary Instruments). PCLSs were incubated in complete RPMI 1640 [10% fetal bovine serum (FBS), 2 mM L-glutamine, penicillin/streptomycin (100 U/ml); Gibco, Life Technologies] for 15 min at 37°C to wash off excess agarose surrounding the tissue. Abs were prepared in complete RPMI 1640, and lung explants were incubated in staining solution for 1.5 hours at 37°C before imaging. Time-lapse videos depicting ILC2 movement were generated over an hour using an inverted laser scanning confocal microscope (SP5, Leica Microsystems). Videos were quantified using Imaris version 8.1 (Bitplane, Oxford Instruments), and ILC2 track speed, track length, and track displacement were quantified using MotilityLab software.

Intravital microscopy

Mouse lung intravital microscopy was performed as previously described (*44*, *66*). Briefly, anesthetized and mechanically ventilated mice were placed on a heat mat in a right lateral position. A small custom-built circular suction chamber was surgically inserted using a small incision between the ribs of the mice for imaging on an upright laser scanning confocal microscope with Hybrid Detectors (Leica SP5). Gentle suction was applied via the vacuum port to

bring the cover slip contained in the chamber into contact with the lung and stabilize the tissue. Time-lapse videos depicting ILC2 movement were generated using 488-, 54-, and 633-nm laser lines through a 0.95 numerical aperture (NA) long working distance water immersion under 25× objective.

Fixed cell/PCLS imaging

Phalloidin-stained ILCs and fixed PCLSs from IL-33 reported mice were imaged using a ZEISS LSM 880 Airyscan nonlinear optics system. DAPI (4′,6-diamidino-2-phenylindole) was excited using a 405-nm diode laser, and phalloidin Alexa Flour 488 was excited at 488 nm using an argon-ion laser, detected using a sub-Airy detector 32-element array (Airyscan), and processed using "auto" 3D Airyscan processing options. Airyscan *z*-stacks were acquired, and Imaris (Bitplane) was used to visualize each cell. SHG signals (produced at a central wavelength of 475 nm) were collected from fixed PCLSs using a Coherent Chameleon Discovery femtosecond pulsed laser tuned to 950 nm and collected using a nondescanned GaAsP detector with 450 ± 50–nm detection filter. A 1.0 NA ZEISS long working distance water immersion under 25× objective was used to collect all images.

SHG analysis

Fifty-micrometer *z*-stacks were imaged over a region of 425.1 μm by 425.1 μm, with at least three stacks per mouse (n = 6 mice per condition). GLCM was performed similar to previous studies (*67*, *68*) Briefly, ImageJ (National Institutes of Health) and the Norwegian University of Life Sciences (UMB) GLCM plugin was used for the texture analysis and modified to run automatically through the four directions, for each of the 100 comparison distances. A maximum projection image was automatically thresholded to produce a mask that was then applied to remove background noise bias in the GLCM analysis by selecting only the collagen SHG signal. The masked image was then passed to the modified GLCM texture plugin. The data files produced were processed using an ImageJ macro to output both the mean and individual values for each texture parameter for each image. These were then imported into Prism (GraphPad), where exponential decay models were fitted to the data.

Cell isolation (BAL, lung, and lung-draining lymph nodes)

The airways were washed three times with 400 μl of PBS, and BAL fluid was collected. After centrifugation of the BAL fluid, supernatants were stored at −80°C for further analysis, and cells were resuspended in 500 μl of complete RPMI 1640 media [10% FBS, 2 mM L-glutamine, penicillin/streptomycin (100 U/ml); Gibco, Life Technologies]. For lung cell isolation, the left lung lobes were cut into small pieces and digested in complete media supplemented with collagenase (type D) (0.15 mg/ml; Roche Diagnostics) and deoxyribonuclease (type 1) (25 μg/ml; Roche Diagnostics) for 1 hour at 37°C. Lung homogenate obtained was then filtered through a 70-μm sieve (BD Biosciences), washed, and resuspended in 1 ml of complete media. Erylysis was performed on 200 μl of whole blood, and leukocytes were washed twice and then resuspended in 1 ml of complete media.

Flow cytometry and intracellular staining

For phenotyping ILC2s in IL-13–eGFP mice by flow cytometry, ILC2s were defined as live, singlet, lymphoid, $GFP^+CD45^+lin^-$ (lineage cocktail: TCRβ, TCRγδ, CD3e, CD5, CD19, CD11b, CD11c, FCεR1, GR-1, F4/80, NKp46, and TER-119), $CD3^-NKp46^-$, and $CD90.2^+/CD127^+/KLRG1^+/CD25^{var}$ cells with positive intracellular IL-13 and IL-5 staining. For intracellular cytokine staining, cells were stimulated with phorbol 12-myristate 13-acetate (Sigma-Aldrich) and ionomycin (EMD Chemicals) in the presence of brefeldin A (Sigma-Aldrich) and incubated for 4 hours at 37°C. After stimulation, cells were washed and incubated for 20 min with anti-CD16/32 (BD Pharmingen) before staining for extracellular antigens in 5% FBS/1% BSA in PBS for 30 min at 4°C. All Abs were purchased from eBioscience (table S2) with the exception of CD31, epithelial cell adhesion molecule (EpCAM), and CD4 (BioLegend) also shown in table S1. After staining for extracellular markers, cells were fixed with intracellular fixation buffer (eBioscience) for 10 min at room temperature. Cells were then washed and stained for intracellular antigens using the Intracellular Fixation and Permeabilization Buffer Set (eBioscience) or the Foxp3/Transcription Factor Staining Buffer Set (eBioscience) for GATA-3 staining. Analysis was performed with LSRFortessa III and cell sorting on FACSAria III (BD Biosciences).

Lung histology and staining

Paraffin-embedded lung sections (4-μm thickness) were stained with hematoxylin and Congo red dyes. Images were taken under polarized light using an upright dry under 40× objective. The number of eosinophils in the peribronchial space was quantified and corrected for the surface area scored.

Human ILC2 bulk cultures

ILC2s were enriched from whole blood using the RosetteSep Human ILC2 Enrichment Kit (STEMCELL Technologies) and further sorted by fluorescence-activated cell sorter using $CD45^+Lin^-$ (CD1a, CD3, CD4, CD5, CD8, CD11c, CD14, CD16, CD19, CD20, CD34, FcγRI, and CD123; BioLegend), $CD161^+$, $CD127^+$, $CRTH2^+$, and C-Kit^{var} (BioLegend). ILC2s were bulk cultured in IL-2, IL-7 (5 ng/ml), and IL-33 (10 ng/ml) (eBioscience), and cytokines and medium were replenished every 3 to 4 days. For investigations involving humans ILC2 isolation, an informed consent was obtained, and the nature and possible consequences of the studies were explained to all donors.

CCR8 Ab blocking and rCCL8 treatment

CCR8 neutralization studies were performed similar to previous reports (*69*). IL-13–eGFP and BALB/c mice were intraperitoneally injected with 5 μg of purified anti-mouse CD198 (CCR8) Ab, (clone: SA214G2) or purified Rat IgG2b, κ Isotype Ctrl Ab 2 days before first dose of rIL-33 treatment and then combined with each of the three rIL-33 doses. Mice were analyzed 24 hours after the third dose. Alternately, 10 μg of recombinant mouse CCL8 (MCP-2; BioLegend) was administered intranasally at the time of the three rIL-33 doses.

BAPN treatment

BAPN treatment was carried out similar to previous reports (*70*). IL-13–eGFP or BALB/c mice were intraperitoneally injected with BAPN (100 mg/kg, Sigma-Aldrich) dissolved in PBS and administered in 200-μl volume on day −1 and then daily for a week over the course of rIL-33 treatment.

Measurement of airway hyperresponsiveness

Airway resistance in mice was evaluated adopting the flexiVent small animal ventilator (SCIREQ) as previously described (*29*). Before procedure, mice were anesthetized with a combination of pentobarbital sodium (50 mg/kg, administered intraperitoneally) and ketamine

(100 mg/kg, administered intramuscularly), tracheostomized, and connected to the flexiVent ventilator using a blunt-ended 19-gauge needle. The mice were ventilated by maintaining an average breathing frequency of 150 breaths/min, a tidal volume of body weight (10 ml/kg), and a positive end-expiratory pressure of about 2 cm H_2O. Differences in resistance to increasing concentrations of nebulized methacholine (3 to 100 mg/ml) were analyzed from the snapshot perturbation measurements. The data were then plotted using multiple linear regression to the single-compartment model in the following form: pressure = resistance × flow + elastance × volume + fitting constant.

Chemotaxis assay

Assays of chemotactic responsiveness were carried out as previously described using 96-well ChemoTx plates with 5-μm pores (Neuro Probe). Migrating cells were detected by the use of CellTiter-Glo Dye (Promega), and resulting luminescence was measured using a TopCount scintillation counter (PerkinElmer). In all experiments, each data point was assayed in duplicate. Data are reported as chemotactic Indices, defined as the migratory response to a particular stimulus divided by the migratory response to media alone.

Analysis of ILC2 dynamics on ECM proteins

Human ILC2s were obtained by sorting and differentiating ILC2s from peripheral blood. ILC2 lines were seeded on tissue culture plates coated with 10% FBS, fibronectin (50 μg/ml), collagen-I, and collagen-IV. Human ILC2 dynamics were imaged on the JuLI imaging system for a period of 12 hours. ILC2 dynamics quantified as changes in speed and displacement were quantified using ImageJ software.

Statistical analysis

All data were analyzed using GraphPad Prism 7. Time-series videos were analyzed, and cell tracks were quantified by Imaris software. Tracks were imported to Prism for quantifying track length and track speed. In addition, tracks were imported into MotilityLab software to display tracks from centroid and differences in mean square displacement. All line graphs and bar charts are expressed as means ± SD, and data were analyzed with nonparametric Mann-Whitney *U* test where significance was defined as $^{*}P < 0.05$, $^{**}P < 0.01$, $^{***}P < 0.001$, and $^{****}P < 0.0001$.

SUPPLEMENTARY MATERIALS

immunology.sciencemag.org/cgi/content/full/4/36/eaav7638/DC1
Fig. S1. Gating strategy for identification of ILC2 populations, related to Fig. 1 (A to C).
Fig. S2. Quantification of ILC2s in different tissues, related to Fig. 1 (A to C).
Fig. S3. Gating strategy for identification of ILC2 populations based on GATA-3 expression, related to Fig. 1 (A to C).
Fig. S4. Distribution of ILC2s and $CD4^+$ T cells in rIL-33–treated mice lungs, related to Fig. 1 (D and F).
Fig. S5. Chemokine receptor expression on ILCs, related to Fig. 4 (A and B).
Fig. S6. Phenotype and IL-13 production by human ILC2 lines, related to Figs. 4 and 5.
Fig. S7. ILC2 motility on ECM proteins, collagen-III, and proteoglycans, versican and tenascin-C, related to Fig. 5 (A to C).
Fig. S8. BAPN fails to affect ILC2 cytokine production and eosinophil movement, related to Fig. 8G.
Table S1. Antibodies used for imaging of PCLS.
Table S2. Antibodies used for flow cytometry.
Table S3. Antibodies used for sorting human ILC2.
Movie S1. Time-lapse imaging of rIL-33–treated mouse lung PCLSs showing ILC2 movement and location, related to Fig. 2A.
Movie S2. Time-lapse imaging of rIL-33–treated mouse lung PCLSs depicting differences in movement of independent ILC2s, related to Fig. 2B.
Movie S3. Time-lapse imaging of rIL-33–treated mouse lung PCLSs depicting high-power videos differences in movement of independent ILC2s, related to Fig. 2C.
Movie S4. Intravital imaging of rIL-33–treated mouse lung depicting amoeboid ILC2 movement, related to Fig. 2H.
Movie S5. Influence of ILC2 survival and cytokines on ILC2 motility, related to Fig. 5 (A to C).
Movie S6. Time-lapse imaging of lung PCLSs from rIL-33–treated mouse treated with anti-CCR8 Ab or isotype Ab, related to Fig. 4I.
Movie S7. Collagen-I–induced ILC2 shape change and elongation of cell body, related to Fig. 5A.
Movie S8. Time-lapse imaging of a lung PCLSs assessing the effect of BAPN on rIL-33–treated mouse lung eosinophil movement, related to Fig. 8G.

REFERENCES AND NOTES

1. M. G. Constantinides, B. D. McDonald, P. A. Verhoef, A. Bendelac, A committed precursor to innate lymphoid cells. *Nature* **508**, 397–401 (2014).
2. N. Serafini, R. G. J. Klein Wolterink, N. Satoh-Takayama, W. Xu, C. A. J. Vosshenrich, R. W. Hendriks, J. P. Di Santo, Gata3 drives development of $ROR\gamma t^+$ group 3 innate lymphoid cells. *J. Exp. Med.* **211**, 199–208 (2014).
3. C. H. Kim, S. Hashimoto-Hill, M. Kim, Migration and tissue tropism of innate lymphoid cells. *Trends Immunol.* **37**, 68–79 (2016).
4. J. K. Bando, H.-E. Liang, R. M. Locksley, Identification and distribution of developing innate lymphoid cells in the fetal mouse intestine. *Nat. Immunol.* **16**, 153–160 (2015).
5. H. Spits, T. Cupedo, Innate lymphoid cells: Emerging insights in development, lineage relationships, and function. *Annu. Rev. Immunol.* **30**, 647–675 (2012).
6. C. S. Klose, D. Artis, Innate lymphoid cells as regulators of immunity, inflammation and tissue homeostasis. *Nat. Immunol.* **17**, 765–774 (2016).
7. A. N. J. McKenzie, H. Spits, G. Eberl, Innate lymphoid cells in inflammation and immunity. *Immunity* **41**, 366–374 (2014).
8. N. Serafini, C. A. J. Vosshenrich, J. P. Di Santo, Transcriptional regulation of innate lymphoid cell fate. *Nat. Rev. Immunol.* **15**, 415–428 (2015).
9. G. F. Sonnenberg, D. Artis, Innate lymphoid cells in the initiation, regulation and resolution of inflammation. *Nat. Med.* **21**, 698–708 (2015).
10. R. Jones, E. J. Cosway, C. Willis, A. J. White, W. E. Jenkinson, H. J. Fehling, G. Anderson, D. R. Withers, Dynamic changes in intrathymic ILC populations during murine neonatal development. *Eur. J. Immunol.* **48**, 1481–1491 (2018).
11. D. Artis, H. Spits, The biology of innate lymphoid cells. *Nature* **517**, 293–301 (2015).
12. G. Eberl, M. Colonna, J. P. Di Santo, A. N. J. McKenzie, Innate lymphoid cells: A new paradigm in immunology. *Science* **348**, aaa6566 (2015).
13. L. A. Monticelli, G. F. Sonnenberg, M. C. Abt, T. Alenghat, C. G. K. Ziegler, T. A. Doering, J. M. Angelosanto, B. J. Laidlaw, C. Y. Yang, T. Sathaliyawala, M. Kubota, D. Turner, J. M. Diamond, A. W. Goldrath, D. L. Farber, R. G. Collman, E. J. Wherry, D. Artis, Innate lymphoid cells promote lung-tissue homeostasis after infection with influenza virus. *Nat. Immunol.* **12**, 1045–1054 (2011).
14. J. C. Nussbaum, S. J. Van Dyken, J. von Moltke, L. E. Cheng, A. Mohapatra, A. B. Molofsky, E. E. Thornton, M. F. Krummel, A. Chawla, H.-E. Liang, R. M. Locksley, Type 2 innate lymphoid cells control eosinophil homeostasis. *Nature* **502**, 245–248 (2013).
15. Y. Huang, K. Mao, X. Chen, M.-a. Sun, T. Kawabe, W. Li, N. Usher, J. Zhu, J. F. Urban Jr., W. E. Paul, R. N. Germain, S1P-dependent interorgan trafficking of group 2 innate lymphoid cells supports host defense. *Science* **359**, 114–119 (2018).
16. G. Gasteiger, X. Fan, S. Dikiy, S. Y. Lee, A. Y. Rudensky, Tissue residency of innate lymphoid cells in lymphoid and nonlymphoid organs. *Science* **350**, 981–985 (2015).
17. H.-K. Kim, S. Lund, R. Baum, P. Rosenthal, N. Khorram, T. A. Doherty, Innate type 2 response to *Alternaria* extract enhances ryegrass-induced lung inflammation. *Int. Arch. Allergy Immunol.* **163**, 92–105 (2014).
18. K. Moro, H. Kabata, M. Tanabe, S. Koga, N. Takeno, M. Mochizuki, K. Fukunaga, K. Asano, T. Betsuyaku, S. Koyasu, Interferon and IL-27 antagonize the function of group 2 innate lymphoid cells and type 2 innate immune responses. *Nat. Immunol.* **17**, 76–86 (2016).
19. A.-H. Lei, Q. Xiao, G.-Y. Liu, K. Shi, Q. Yang, X. Li, Y.-F. Liu, H.-K. Wang, W.-P. Cai, Y.-J. Guan, D. I. Gabrilovich, J. Zhou, ICAM-1 controls development and function of ILC2. *J. Exp. Med.* **215**, 2157–2174 (2018).
20. T. A. Doherty, D. Scott, H. H. Walford, N. Khorram, S. Lund, R. Baum, J. Chang, P. Rosenthal, A. Beppu, M. Miller, D. H. Broide, Allergen challenge in allergic rhinitis rapidly induces increased peripheral blood type 2 innate lymphoid cells that express CD84. *J. Allergy Clin. Immunol.* **133**, 1203–1205.e7 (2014).
21. J. L. Barlow, A. Bellosi, C. S. Hardman, L. F. Drynan, S. H. Wong, J. P. Cruickshank, A. N. J. McKenzie, Innate IL-13–producing nuocytes arise during allergic lung inflammation and contribute to airways hyperreactivity. *J. Allergy Clin. Immunol.* **129**, 191–198.e4 (2012).
22. K. R. Bartemes, K. Iijima, T. Kobayashi, G. M. Kephart, A. N. McKenzie, H. Kita, IL-33–responsive $lineage^-CD25^+CD44^{hi}$ lymphoid cells mediate innate type 2 immunity and allergic inflammation in the lungs. *J. Immunol.* **188**, 1503–1513 (2012).
23. K. R. Bartemes, G. M. Kephart, S. J. Fox, H. Kita, Enhanced innate type 2 immune response in peripheral blood from patients with asthma. *J. Allergy Clin. Immunol.* **134**, 671–678.e4 (2014).

24. S. G. Smith, R. Chen, M. Kjarsgaard, C. Huang, J.-P. Oliveria, P. M. O'Byrne, G. M. Gauvreau, L.-P. Boulet, C. Lemiere, J. Martin, P. Nair, R. Sehmi, Increased numbers of activated group 2 innate lymphoid cells in the airways of patients with severe asthma and persistent airway eosinophilia. *J. Allergy Clin. Immunol.* **137**, 75–86.e8 (2016).
25. M. Ebbo, A. Crinier, F. Vely, E. Vivier, Innate lymphoid cells: Major players in inflammatory diseases. *Nat. Rev. Immunol.* **17**, 665–678 (2017).
26. P. Licona-Limón, L. K. Kim, N. W. Palm, R. A. Flavell, T_H2, allergy and group 2 innate lymphoid cells. *Nat. Immunol.* **14**, 536–542 (2013).
27. K. Moro, T. Yamada, M. Tanabe, T. Takeuchi, T. Ikawa, H. Kawamoto, J. Furusawa, M. Ohtani, H. Fujii, S. Koyasu, Innate production of T_H2 cytokines by adipose tissue-associated c-Kit$^+$Sca-1$^+$ lymphoid cells. *Nature* **463**, 540–544 (2010).
28. D. R. Neill, S. H. Wong, A. Bellosi, R. J. Flynn, M. Daly, T. K. A. Langford, C. Bucks, C. M. Kane, P. G. Fallon, R. Pannell, H. E. Jolin, A. N. J. McKenzie, Nuocytes represent a new innate effector leukocyte that mediates type-2 immunity. *Nature* **464**, 1367–1370 (2010).
29. A. E. Price, H.-E. Liang, B. M. Sullivan, R. L. Reinhardt, C. J. Eisley, D. J. Erle, R. M. Locksley, Systemically dispersed innate IL-13–expressing cells in type 2 immunity. *Proc. Natl. Acad. Sci. U.S.A.* **107**, 11489–11494 (2010).
30. T. A. Doherty, N. Khorram, S. Lund, A. K. Mehta, M. Croft, D. H. Broide, Lung type 2 innate lymphoid cells express cysteinyl leukotriene receptor 1, which regulates T_H2 cytokine production. *J. Allergy Clin. Immunol.* **132**, 205–213 (2013).
31. E. D. Wojno, L. A. Monticelli, S. V. Tran, T. Alenghat, L. C. Osborne, J. J. Thome, C. Willis, A. Budelsky, D. L. Farber, D. Artis, The prostaglandin D_2 receptor CRTH2 regulates accumulation of group 2 innate lymphoid cells in the inflamed lung. *Mucosal Immunol.* **8**, 1313–1323 (2015).
32. W. Zhou, S. Toki, J. Zhang, K. Goleniewksa, D. C. Newcomb, J. Y. Cephus, D. E. Dulek, M. H. Bloodworth, M. T. Stier, V. Polosuhkin, R. D. Gangula, S. A. Mallal, D. H. Broide, R. S. Peebles Jr., Prostaglandin I_2 signaling and inhibition of group 2 innate lymphoid cell responses. *Am. J. Respir. Crit. Care Med.* **193**, 31–42 (2016).
33. J. Maric, A. Ravindran, L. Mazzurana, A. K. Björklund, A. Van Acker, A. Rao, D. Friberg, S.-E. Dahlén, A. Heinemann, V. Konya, J. Mjösberg, Prostaglandin E2 suppresses human group 2 innate lymphoid cell function. *J. Allergy Clin. Immunol.* **141**, 1761–1773.e6 (2018).
34. L. Denney, A. J. Byrne, T. J. Shea, J. S. Buckley, J. E. Pease, G. M. F. Herledan, S. A. Walker, L. G. Gregory, C. M. Lloyd, Pulmonary epithelial cell-derived cytokine TGF-β1 is a critical cofactor for enhanced innate lymphoid cell function. *Immunity* **43**, 945–958 (2015).
35. T. Lämmermann, R. N. Germain, The multiple faces of leukocyte interstitial migration. *Semin. Immunopathol.* **36**, 227–251 (2014).
36. M. H. Kim, E. J. Taparowsky, C. H. Kim, Retinoic acid differentially regulates the migration of innate lymphoid cell subsets to the gut. *Immunity* **43**, 107–119 (2015).
37. M. Salimi, J. L. Barlow, S. P. Saunders, L. Xue, D. Gutowska-Owsiak, X. Wang, L.-C. Huang, D. Johnson, S. T. Scanlon, A. N. J. McKenzie, P. G. Fallon, G. S. Ogg, A role for IL-25 and IL-33–driven type-2 innate lymphoid cells in atopic dermatitis. *J. Exp. Med.* **210**, 2939–2950 (2013).
38. B. Roediger, R. Kyle, K. H. Yip, N. Sumaria, T. V. Guy, B. S. Kim, A. J. Mitchell, S. S. Tay, R. Jain, E. Forbes-Blom, X. Chen, P. L. Tong, H. A. Bolton, D. Artis, W. E. Paul, B. Fazekas de St Groth, M. A. Grimbaldeston, G. Le Gros, W. Weninger, Cutaneous immunosurveillance and regulation of inflammation by group 2 innate lymphoid cells. *Nat. Immunol.* **14**, 564–573 (2013).
39. M. R. Karta, P. S. Rosenthal, A. Beppu, C. Y. Vuong, M. Miller, S. Das, R. C. Kurten, T. A. Doherty, D. H. Broide, β_2 integrins rather than β_1 integrins mediate *Alternaria*-induced group 2 innate lymphoid cell trafficking to the lung. *J. Allergy Clin. Immunol.* **141**, 329–338.e12 (2018).
40. R. R. Ricardo-Gonzalez, S. J. Van Dyken, C. Schneider, J. Lee, J. C. Nussbaum, H.-E. Liang, D. Vaka, W. L. Eckalbar, A. B. Molofsky, D. J. Erle, R. M. Locksley, Tissue signals imprint ILC2 identity with anticipatory function. *Nat. Immunol.* **19**, 1093–1099 (2018).
41. M. F. Krummel, F. Bartumeus, A. Gérard, T cell migration, search strategies and mechanisms. *Nat. Rev. Immunol.* **16**, 193–201 (2016).
42. Y. Kondo, T. Yoshimoto, K. Yasuda, S. Futatsugi-Yumikura, M. Morimoto, N. Hayashi, T. Hoshino, J. Fujimoto, K. Nakanishi, Administration of IL-33 induces airway hyperresponsiveness and goblet cell hyperplasia in the lungs in the absence of adaptive immune system. *Int. Immunol.* **20**, 791–800 (2008).
43. S. Boitano, A. N. Flynn, C. L. Sherwood, S. M. Schulz, J. Hoffman, I. Gruzinova, M. O. Daines, *Alternaria alternata* serine proteases induce lung inflammation and airway epithelial cell activation via PAR_2. *Am. J. Physiol. Lung Cell. Mol. Physiol.* **300**, L605–L614 (2011).
44. M. B. Headley, A. Bins, A. Nip, E. W. Roberts, M. R. Looney, A. Gerard, M. F. Krummel, Visualization of immediate immune responses to pioneer metastatic cells in the lung. *Nature* **531**, 513–517 (2016).
45. M. A. Schaller, L. E. Kallal, N. W. Lukacs, A key role for CC chemokine receptor 1 in T-cell-mediated respiratory inflammation. *Am. J. Pathol.* **172**, 386–394 (2008).
46. S. A. Islam, D. S. Chang, R. A. Colvin, M. H. Byrne, M. L. McCully, B. Moser, S. A. Lira, I. F. Charo, A. D. Luster, Mouse CCL8, a CCR8 agonist, promotes atopic dermatitis by recruiting IL-5$^+$ T_H2 cells. *Nat. Immunol.* **12**, 167–177 (2011).
47. W. Xu, J. P. Di Santo, Taming the beast within: Regulation of innate lymphoid cell homeostasis and function. *J. Immunol.* **191**, 4489–4496 (2013).
48. L. Xue, M. Salimi, I. Panse, J. M. Mjösberg, A. N. J. McKenzie, H. Spits, P. Klenerman, G. Ogg, Prostaglandin D_2 activates group 2 innate lymphoid cells through chemoattractant receptor-homologous molecule expressed on T_H2 cells. *J. Allergy Clin. Immunol.* **133**, 1184–1194.e7 (2014).
49. L. G. Gregory, S. A. Mathie, S. A. Walker, S. Pegorier, C. P. Jones, C. M. Lloyd, Overexpression of Smad2 drives house dust mite–mediated airway remodeling and airway hyperresponsiveness via activin and IL-25. *Am. J. Respir. Crit. Care Med.* **182**, 143–154 (2010).
50. G. J. Laurent, Lung collagen: More than scaffolding. *Thorax* **41**, 418–428 (1986).
51. A. Andersson-Sjöland, O. Hallgren, S. Rolandsson, M. Weitoft, E. Tykesson, A.-K. Larsson-Callerfelt, K. Rydell-Törmänen, L. Bjermer, A. Malmström, J. C. Karlsson, G. Westergren-Thorsson, Versican in inflammation and tissue remodeling: The impact on lung disorders. *Glycobiology* **25**, 243–251 (2015).
52. R. Cicchi, D. Kapsokalyvas, V. De Giorgi, V. Maio, A. Van Wiechen, D. Massi, T. Lotti, F. S. Pavone, Scoring of collagen organization in healthy and diseased human dermis by multiphoton microscopy. *J. Biophotonics* **3**, 34–43 (2010).
53. C. Vennin, V. T. Chin, S. C. Warren, M. C. Lucas, D. Herrmann, A. Magenau, P. Melenec, S. N. Walters, G. del Monte-Nieto, J. R. W. Conway, M. Nobis, A. H. Allam, R. A. McCloy, N. Currey, M. Pinese, A. Boulghourjian, A. Zaratzian, A. A. S. Adam, C. Heu, A. M. Nagrial, A. Chou, A. Steinmann, A. Drury, D. Froio, M. Giry-Laterriere, N. L. E. Harris, T. Phan, R. Jain, W. Weninger, E. J. McGhee, R. Whan, A. L. Johns, J. S. Samra, L. Chantrill, A. J. Gill, M. Kohonen-Corish, R. P. Harvey, A. V. Biankin, I. Australian Pancreatic Cancer Genome, T. R. J. Evans, K. I. Anderson, S. T. Grey, C. J. Ormandy, D. Gallego-Ortega, Y. Wang, M. S. Samuel, O. J. Sansom, A. Burgess, T. R. Cox, J. P. Morton, M. Pajic, P. Timpson, Transient tissue priming via ROCK inhibition uncouples pancreatic cancer progression, sensitivity to chemotherapy, and metastasis. *Sci. Transl. Med.* **9**, eaai8504 (2017).
54. A. Leithner, A. Eichner, J. Müller, A. Reversat, M. Brown, J. Schwarz, J. Merrin, D. J. J. de Gorter, F. Schur, J. Bayerl, I. de Vries, S. Wieser, R. Hauschild, F. P. L. Lai, M. Moser, D. Kerjaschki, K. Rottner, J. V. Small, T. E. B. Stradal, M. Sixt, Diversified actin protrusions promote environmental exploration but are dispensable for locomotion of leukocytes. *Nat. Cell Biol.* **18**, 1253–1259 (2016).
55. P. Friedl, S. Borgmann, E.-B. Bröcker, Amoeboid leukocyte crawling through extracellular matrix: Lessons from the *Dictyostelium* paradigm of cell movement. *J. Leukoc. Biol.* **70**, 491–509 (2001).
56. T. Lämmermann, M. Sixt, Mechanical modes of 'amoeboid' cell migration. *Curr. Opin. Cell Biol.* **21**, 636–644 (2009).
57. N. J. Kenyon, R. W. Ward, G. McGrew, J. A. Last, TGF-β_1 causes airway fibrosis and increased collagen I and III mRNA in mice. *Thorax* **58**, 772–777 (2003).
58. T. Honda, J. G. Egen, T. Lämmermann, W. Kastenmüller, P. Torabi-Parizi, R. N. Germain, Tuning of antigen sensitivity by T cell receptor-dependent negative feedback controls T cell effector function in inflamed tissues. *Immunity* **40**, 235–247 (2014).
59. M. T. Stier, J. Zhang, K. Goleniewska, J. Y. Cephus, M. Rusznak, L. Wu, L. Van Kaer, B. Zhou, D. C. Newcomb, R. S. Peebles Jr., IL-33 promotes the egress of group 2 innate lymphoid cells from the bone marrow. *J. Exp. Med.* **215**, 263–281 (2018).
60. R. Sumagin, H. Prizant, E. Lomakina, R. E. Waugh, I. H. Sarelius, LFA-1 and Mac-1 define characteristically different intralumenal crawling and emigration patterns for monocytes and neutrophils in situ. *J. Immunol.* **185**, 7057–7066 (2010).
61. J. von Moltke, M. Pepper, Sentinels of the type 2 immune response. *Trends Immunol.* **39**, 99–111 (2018).
62. S. A. Islam, A. D. Luster, T cell homing to epithelial barriers in allergic disease. *Nat. Med.* **18**, 705–715 (2012).
63. M. Barczyk, S. Carracedo, D. Gullberg, Integrins. *Cell Tissue Res.* **339**, 269–280 (2010).
64. J.-F. Moreau, T. Pradeu, A. Grignolio, C. Nardini, F. Castiglione, P. Tieri, M. Capri, S. Salvioli, J.-L. Taupin, P. Garagnani, C. Franceschi, The emerging role of ECM crosslinking in T cell mobility as a hallmark of immunosenescence in humans. *Ageing Res. Rev.* **35**, 322–335 (2017).
65. G. Burgstaller, S. Vierkotten, M. Lindner, M. Königshoff, O. Eickelberg, Multidimensional immunolabeling and 4D time-lapse imaging of vital ex vivo lung tissue. *Am. J. Physiol. Lung Cell. Mol. Physiol.* **309**, L323–L332 (2015).
66. M. R. Looney, E. E. Thornton, D. Sen, W. J. Lamm, R. W. Glenny, M. F. Krummel, Stabilized imaging of immune surveillance in the mouse lung. *Nat. Methods* **8**, 91–96 (2011).
67. B. W. Miller, J. P. Morton, M. Pinese, G. Saturno, N. B. Jamieson, E. McGhee, P. Timpson, J. Leach, L. McGarry, E. Shanks, P. Bailey, D. Chang, K. Oien, S. Karim, A. Au, C. Steele, C. R. Carter, C. McKay, K. Anderson, T. R. J. Evans, R. Marais, C. Springer, A. Biankin, J. T. Erler, O. J. Sansom, Targeting the LOX/hypoxia axis reverses many of the features that make pancreatic cancer deadly: Inhibition of LOX abrogates metastasis and enhances drug efficacy. *EMBO Mol. Med.* **7**, 1063–1076 (2015).
68. N. Rath, J. P. Morton, L. Julian, L. Helbig, S. Kadir, E. J. McGhee, K. I. Anderson, G. Kalna, M. Mullin, A. V. Pinho, I. Rooman, M. S. Samuel, M. F. Olson, ROCK signaling promotes collagen remodeling to facilitate invasive pancreatic ductal adenocarcinoma tumor cell growth. *EMBO Mol. Med.* **9**, 198–218 (2017).

69. D. O. Villarreal, A. L'Huillier, S. Armington, C. Mottershead, E. V. Filippova, B. D. Coder, R. G. Petit, M. F. Princiotta, Targeting CCR8 induces protective antitumor immunity and enhances vaccine-induced responses in colon cancer. *Cancer Res.* **78**, 5340–5348 (2018).
70. T. Cheng, Q. Liu, R. Zhang, Y. Zhang, J. Chen, R. Yu, G. Ge, Lysyl oxidase promotes bleomycin-induced lung fibrosis through modulating inflammation. *J. Mol. Cell Biol.* **6**, 506–515 (2014).

Acknowledgments: We thank S. Rothery, D. Gaboriau, and A. Bruckbauer from the FILM facility (in part funded by Wellcome Trust grant 104931/Z/14/Z), and Core Services and Advanced Technologies at the Cancer Research UK Beatson Institute (C596/A17196), with particular thanks to the Beatson Advanced Imaging Resource. We also thank J. Srivastava and J. Rowley of the Imperial College Core Flow Cytometry facility for assistance with flow cytometry and L. Lawrence for histological sectioning. We also thank D. Patel, H. Stoelting, N. En Chan, and M. Mc Fie for expert technical assistance. We also acknowledge L. Robson for thorough maintenance of the human ILC2 lines. We additionally thank C. Winchester for editing our manuscript. Last, we acknowledge MotilityLab for providing the resource for carrying out our analysis on ILC2 dynamics. **Funding:** L.M.C. thanks the MRC (MR/M01245X/1) and Cancer Research UK (core funding A23983 and A17196). This study was funded by the Wellcome Trust grant 107059/Z/15/Z, awarded to C.M.L., who is a Wellcome Senior Fellow in Basic Biomedical Sciences. **Author contributions:** C.M.L. conceived the idea and directed the study. S.A.W. performed and analyzed the lung function experiments. L.M.C. provided expertise in imaging techniques. J.E.P. provided expert advice on chemotaxis assays. M.B.H. and M.F.K. provided expert advice on intravital imaging. F.P., L.D., L.G.G., L.M.C., and C.M.L. wrote the manuscript. F.P. and L.D. designed experiments. F.P., L.D., L.J.E., L.M.C., J.V., and R.O. performed experiments. F.P., E.J.M., L.M.C., and L.D. analyzed data. F.P., E.J.M., L.M.C., and L.D. generated figures. R.O. maintained and genotyped mouse lines. **Competing interests:** The authors declare that they have no competing interest. **Data and materials availability:** All data needed to evaluate the conclusions of the paper are present in the paper or the Supplementary Materials.

Submitted 17 October 2018
Accepted 9 April 2019
Published 7 June 2019
10.1126/sciimmunol.aav7638

Citation: F. Puttur, L. Denney, L. G. Gregory, J. Vuononvirta, R. Oliver, L. J. Entwistle, S. A. Walker, M. B. Headley, E. J. McGhee, J. E. Pease, M. F. Krummel, L. M. Carlin, C. M. Lloyd, Pulmonary environmental cues drive group 2 innate lymphoid cell dynamics in mice and humans. *Sci. Immunol.* **4**, eaav7638 (2019).

Science Immunology

Pulmonary environmental cues drive group 2 innate lymphoid cell dynamics in mice and humans

Franz Puttur, Laura Denney, Lisa G. Gregory, Juho Vuononvirta, Robert Oliver, Lewis J. Entwistle, Simone A. Walker, Mark B. Headley, Ewan J. McGhee, James E. Pease, Matthew F. Krummel, Leo M. Carlin and Clare M. Lloyd

Sci. Immunol. **4**, eaav7638.
DOI: 10.1126/sciimmunol.aav7638

Filming the airways

Group 2 innate lymphoid cells (ILC2s) are key drivers of immune responses in the lung. Using an interleukin-13 (IL-13) reporter mouse strain in conjunction with sophisticated microscopy, Puttur *et al*. have visualized migration of ILC2s in allergic airway inflammation. They report that ILC2s exhibit dynamic ameboid-like movement in response to IL-33 and that IL-33–induced up-regulation of chemokine receptor 8 on ILC2s promotes homing of ILC2s to deposits of chemokine ligand 8 within the airways. They also found a role for collagen-I, a component of the extracellular matrix (ECM) in directly regulating migration of ILC2s. The study underscores the importance of how structural cues from the ECM work in conjunction with immune mediators to influence immune cell functions in tissues.